High-resolution vasomotion analysis reveals novel venous physiological features and progressive modulation of cerebral vascular networks by stroke

Yiyi Zhang[1,2,#], Jinze Li[2,#], Huiqi Xie[2], Yuxiao Jin[2], Wentao Wang[2], Bingrui Zhao[2], Jie-Min Jia[2,3,4,*]

[1]Zhejiang University, Hangzhou 3000124, China.

[2]Key Laboratory of Growth Regulation and Translation Research of Zhejiang Province, School of Life Sciences, Westlake University, Hangzhou, Zhejiang 310024, China;

[3]Institute of Basic Medical Sciences, Westlake Institute for Advanced Study, Hangzhou, Zhejiang 310024, China;

[4]Westlake Laboratory of Life Sciences and Biomedicine, Hangzhou, Zhejiang 310024, China.

[#] **Equally contribute to this work**

***Correspondence:** jiajiemin@westlake.edu.cn

Abstract

Spontaneous cerebral vasomotion, characterized by ~0.1 Hz rhythmic contractility, is crucial for brain homeostasis. However, our understanding of vasomotion is limited due to a lack of high-precision analytical methods to determine single vasomotion events at basal levels. Here, we developed a novel strategy that integrates a baseline smoothing algorithm, allowing precise measurements of vasodynamics and concomitant Ca^{2+} dynamics in mouse cerebrovasculature imaged by two-photon microscopy. We identified several previously unrecognized vasomotion properties under different physiological and pathological conditions especially in ischemic stroke which is a frequently occurring and highly harmful brain disease result in brain damage and significant neurological impairments that originates from vessel occlusion. First, venules exhibit motion with a ~0.1-Hz peak in the power spectrum; energy at this frequency is depleted by anesthetics, signifying a novel aspect of venule physiology related to basal neural activity. Second, compared to previous diameter-based estimations, our radius-based measurements reveal nonisotropic vascular movements, enabling a more precise determination of the latency between smooth muscle cell (SMC) Ca^{2+} activity and vasocontraction. Third, Ca^{2+} dynamics were larger in venular pericytes than in arteriolar SMCs while unrelated to venule vasomotion. Fourth, we characterized single vasomotion event kinetics at scales of less than 4 seconds. Finally, following pathological vasoconstrictions induced by ischemic stroke, vasoactive arterioles transitioned to an inert state and persisted despite recanalization. In summary, we developed a highly accurate technique for analyzing spontaneous vasomotion, and we suggest a potential strategy to reduce stroke damage by promoting vasomotion recovery.

Introduction

Vasomotion has been described as vascular smooth muscle cell (SMC)-initiated spontaneous oscillation that happen relatively independent of pulsatile blood flow[1, 2]. It is characterized by 0.1 Hz sinusoidal changes in vessel diameter[3-5], regulates cerebral blood flow[6, 7](CBF) and has important functions in multiple organs[8-14]. Spontaneous vasomotion influences both the central nervous system and peripheral systems. In the central nervous system, vasomotion reflecting basal fluctuations in blood oxygenation is related to resting-state neural activity[14, 15]. Recently, vascular optogenetics revealed that enhanced vasomotor activity promotes cerebral spinal fluid influx to the brain parenchyma[16]. Furthermore, mechanical forces generated by vasomotion can serve as regulatory signals to nearby mechanic-sensing astrocytes[17]. As for the peripheral systems, vasomotion modulates fluid filtration pressure in the pulmonary vessels and promotes interstitial fluid clearance in rabbit ear skin[18, 19]. Moreover, the importance of vasomotion for tissue metabolism has been demonstrated in studies on the testes, showing that vasomotion is essential for normal function[20-22]. These findings highlight the importance of spontaneous vasomotion in tissue homeostasis in both peripheral and central systems.

Vasomotion dysfunction is associated with neuropathies[14, 23] and oscillatory blood flow at 0.1 Hz has been shown to promote cerebral tissue oxygenation during reduced CBF in human in clinical trials and under high-altitude conditions[24, 25]. Moreover, vasomotion as a driving force can facilitate cerebral paravascular clearance of metabolic waste which is particularly important for elucidating the pathogenesis of Alzheimer's disease (AD)[14, 15]. These findings highlight that vasomotion is an important new area of research that may support the development of

therapeutics for brain diseases such as stroke, AD, and vascular dementia[26].

However, our current understanding of cerebral vasomotion is not comprehensive. For the generation of vasomotion, the presence of a cellular oscillator is necessary which can normally be visualized under experimental conditions in form of intracellular Ca^{2+} transients[27]. In the central nervous system, SMCs with synchronized Ca^{2+} fluctuations[28] are responsible for the self-generated movement component of vasomotion, which is independent of external factors such as respiratory rhythms and heart beats[1, 28, 29]. Therefore, it is crucial to explore the correlation and time delay between fluctuation SMC calcium and arteriolar vasomotion for research connections of mural cell and vessel. The variation of vessel diameter over time is commonly used to characterize vasomotion, while the vessel diameter is defined as distance between bilateral vessel walls and calculated using the half width half maximum (FWHM) methods[30]. A recently developed vasomotion index integrates multiple features of vasomotion into one general parameter by calculating the area under the diameter-change curve over time (time domain); however, this method is not precise enough in characterizing vasomotion and cannot identify individual events[6]. Moreover, the research on vasomotion focuses on the attributes in the frequency domain due to the complexity of the time domain representation of vasomotion signals[14, 31]. In summary, important aspects of vasomotion, such as single vasomotion event determination, event duration and kinetics, and the time delay between SMC Ca^{2+} elevation and arteriolar contraction, remain uncharacterized. Conventional analytical approaches using the frequency and time domains are inadequate for investigating these factors. A suitable baseline should be established for basal vasomotion investigations to achieve normalization of vasomotion comparison both in physiological and pathological states; however, this has not yet been achieved. For instance, neither the baseline calculated by the smallest observed diameter (D_0 minimal) nor that calculated by the average diameter (D_0 average) is able to distinguish vasomotion events under resting-state due to insensitive baseline threshold, although they are frequently used to differentiate large vasomotion signals under a series of stimulation paradigms[32, 33].

In cerebral vasomotion field, research on venules is still incomplete, the prevailing view is that venular vasomotion is scarce[3, 14, 30]. However, this perceived scarcity either reflects the genuine nature of vasomotion in cerebral venules or is falsely observed due to limitations with current techniques, as few specialized techniques have been developed. In addition, most associations between vasomotion and pathological conditions are based on arteriole studies, and the extent of venular network involvement remains unknown. Understanding venule vasomotion is crucial, given the importance of venules as integral components of the circulatory system[34].

Ischemic stroke is a leading cause of mortality and disability worldwide, characterized by the sudden interruption of blood flow to the brain, resulting in severe neurological deficits. It is a brain condition caused by vessel occlusion. Vasodynamic deficits after successful recanalization have been linked to stroke recurrence and poor recovery after stroke[35]. Mouse models have consistently demonstrated pathological SMC constrictions during occlusion that prevent re-establishment of blood flow[36]. This pathological constriction occurs immediately after the initiation of spreading depolarization (SD) during the hyperacute ischemic phase. However, whether this early SMC constriction leads to secondary, prolonged SMC functional deficits during vasomotion has yet to be determined. Understanding this pathological progression may

elucidate stroke characteristics, leading to the development of new methods to prevent delayed neural damage progression.

Here, we integrated multiple algorithms to develop a high-precision analytical method, allowing the quantification of various indices related to spontaneous vasomotion. These algorithms include vasomotion and calcium kinetics identification through the F_0 smoothing algorithm combined with outlier detection, vessel radius definition and calculation based on the full width at half maximum (FHWM) and least-square method, time-series curve similarity comparisons through dynamic time warping (DTW), time lag estimation between SMC calcium fluctuations and vasomotion based on sliding cross-correlation values, and arteriolar propagation index quantification through correlation coefficient (CC) maps. This method replicated known vasomotion properties and showed more robust and comprehensive characterization indicators for vasomotion. With this novel method, we determined that cerebral venules exhibit vasomotion that is fully diminished under anesthesia. Moreover, we identified single vasomotion event kinetics (lasting only 2–3 seconds) and found a shorter latency than previously known between Ca^{2+} increase and arteriole contraction. Furthermore, we identified the cessation of arteriole vasomotion after stroke. Our results have gained a deeper understanding of vasomotion, and have direct implications for research to cerebral vessel networks and ischemic stroke characteristics.

Results

A high-precision analytical method for vasomotion and achieved parameters.

In order to perform a comprehensive description of vasomotion, we obtained various vasomotion parameters through eight steps. We first got an overview of vascular networks through a cranial window in head-fixed, awake adult C57/BL6J mice (Step 1 in Fig. 1). We performed two-photon imaging at least two weeks after cranial surgery to prevent any side effects related to vessel potential from acute inflammation. A cranial window was created above the somatosensory cortex in every mouse, which includes distal branches of the middle cerebral artery. Time-lapse planar imaging was performed over a 216-second or 320-second period (200-point length), with a scanning rate of 0.926 or 0.625 Hz, unless otherwise indicated.

In this study, we focused on the pial arteriolar and venular networks, which are known to exhibit distinct vasomotor activity. The identification of these networks was facilitated by the distinctive morphological characteristics of their mural cells, which were demonstrated in Rosa26-reporter mice crossed with *SMACreER* mice. Specifically, the tamoxifen-inducible expression of Cre under control of the SMA promoter allowed for the labeling of nearly all arterioles and a very small proportion of large venules (> 100 μm, Supplemental Fig. 1). The reporter mice used in our study included Ai14, Ai47, and Ai96 mice; in the presence of Cre activity, the SMCs in these mice express tdTomato, EGFP, and GCaMP6s. Intriguingly, our observations consistently revealed that arterioles were positioned above venules when they intersected spatially. This phenomenon was also observed in *SMACreER:Rosa26*-reporter mice (Supplementary Fig. 1A, Movie 1). Consequently, this characteristic allowed us to reliably distinguish pial arterioles from venules in wild-type mice that received intraluminal dye injections.

Next, we performed an eight-step process to analyze the time-lapse images and assessed nine parameters related to spontaneous vasomotion, as specified below. In step 1, we generated a time-stack kymograph for each vascular segment utilizing the reslice function in

ImageJ with linear regions of interest (ROIs) that were strictly perpendicular to the longitudinal axis of the targeted vessel (lines in Step 1 in Fig. 1 and Supplementary Fig. 1B). Only well-focused vessel segments were chosen for vasomotion analysis, accounting for the curvature of pial vessels and excluding all out-of-focus vessels (Supplementary Fig. 2). This criterion is important for accurate vasomotion studies.

In step 2, we digitized the brightness of each pixel along each horizontal line in the kymograph to form a time stack matrix of the image, and the image stacks were processed in MATLAB with Gaussian filtering to reduce spatial noise. For example, in our case, we considered 100 horizontal lines spanning a total of 108 seconds, with representative digitized brightness changes shown in blue, purple, and green for the first three horizontal lines (Fig. 1).

In step 3, we determined the diameter as the FWHM of the brightness line profile. We identified vascular boundaries on both sides of each vessel through grayscale differences (Step 3.1) and generated a smoothed curve representing the boundaries by utilizing Monotone piecewise cubic interpolation (Pchip) based on Hermite interpolation (Step 3.2). Consequently, we determined the half-height coordinates of both boundaries to calculate the vessel diameter for each image stack (Step 3.3) and digitally assessed dynamic variations in vessel diameter over time (Step 4).

In steps 5 and 6, the baseline diameter (D_0) variation over time was calculated using the D_0 smoothing method. Initially, we adopted three methods that are commonly used to determine the baselines of the time series of the Ca^{2+} fluorescence (F) intensity fluctuations in neurons under stimulated conditions, namely, F_0 average, F_0 minimal, and F_0 smooth[37]. The last method requires a time-rolling algorithm, while the first two methods simply use the average change or the smallest change as a baseline. Under basal conditions with no external stimulation, vasomotion events are difficult to differentiate with two methods that generate a fixed baseline (D_0 minimal and average) when applying the usual criterion for identifying a signal, namely, that the signal should exceed twice the standard deviation (SD) of the diameter curve (Supplementary Fig. 3). In contrast, we detected more peaks (D_{1n}-D_{0n} > 2*SD) when we employed the D_0 smoothing method, a sliding window approach. We used a window width of forty frames and applied the eighth smallest number in each window to generate a variable D_0 baseline (time-rolling approach), referred to as the "smooth baseline". Additionally, to minimize the number of false positives (step 7), we filtered the above results by selecting one event when two events were detected within three consecutive frames. To our knowledge, we are the first to utilize the time-rolling strategy in basal vasomotion analysis.

In addition, we applied traditional frequency and time domain analysis approaches to quantify nine parameters of spontaneous vasomotion events (Fig. 1), including kymographs (Parameter 1), time series of the diameter ratio change (Parameter 2), and spectral analyses of the diameter change curve (Parameter 3). Vasomotion can be divided into five components: the frequency of vasomotion (Parameter 4), the standard deviation of the time interval between two adjacent events (Parameter 5), the absolute difference in the vascular diameter change (ΔD, calculated as D_n-D_0, Parameter 6), the amplitude ratio of the vasomotion ($\Delta D/D_0$, Parameter 7), and the average diameter of the vessel (Parameters 8). Importantly, a novel contribution by elucidating the vasomotion dynamics, introducing for the first time the concept of single vasomotion cycles (Parameter 9). In summary, we developed a procedure to comprehensively quantify spontaneous cerebral vasomotion events with high precision.

Freshly dissected mouse brains exhibit altered but noticeable arteriolar spontaneous vasomotion

To study vasomotion dynamics of arterioles, we compare arteriolar vasomotion index between freshly dissected mouse brains and awake mouse brain. Although isolated arterioles contract in vitro due to SMC-generated myogenic forces[38], two key uncertainties remain in the ex vivo brain. Firstly, it is unclear whether the ex vivo vasomotion resembles the ~ 0.1-Hz vasomotion in awake brains. Secondly, the duration and quantitative differences of ex vivo vasomotion compared to in vivo vasomotion are still unknown. We obtained vasodynamics data through two-photon microscopy, examining both freshly dissected mouse brains and head-fixed awake mice positioned on a treadmill with a surgically opened cranial window (Figure 2A). Ultimately, the effectiveness of the vasomotion properties described in Figure 1 will be assessed by comparing these two conditions.

Pial arterioles were identified through two methods: staining with the mitochondria dye TMRM, which exhibited a noticeably higher fluorescent intensity in SMCs, or by utilizing *SMACreER:Ai14* mice (Fig. 2B). We focused on the downstream vascular tree of the middle cerebral artery, ensuring consistent distances between the experimental conditions.

The kymographs generated in blue lines revealed differences in vasomotion profile under these two conditions (Fig. 2B, Movie 2-3). The time series of $\Delta D/D_0$ further corroborated this disparity (Fig. 2C). Although different in these aspects, Fourier analysis revealed that dissected brains kept in artificial cerebrospinal fluid (ACSF) for two hours without an external supply of oxygen resembled characteristic peaks around 0.1 Hz observed in vivo (Fig. 2D). The vasomotion index analyses indicated that all four aspects of vasodynamics robustly decreased in ex vivo brains (Fig. 2E). Altogether, these data not only demonstrate that the local control of SMCs over arteriole diameter can be up to two hours ex vivo but also support that the present vasomotion analyses sufficiently precise to discern differential vasomotion characteristics under different conditions.

Vasodynamic changes derived from both internal and external diameters can be used to characterize spontaneous vasomotion.

Depending on the specific experimental conditions, some previous reports have focused on internal diameter[14, 39, 40], while others have measured external diameter[6, 41]. Consequently, we considered whether the vasomotion features extracted from these two diameters are comparable. To measure these features simultaneously, we employed *SMACreER:Rosa26* reporter mice injected with intravascular rhodamine or FITC dyes. We standardized the representations of the SMCs, where all subsequent figures utilize green color to represent the external diameter and red color to represent measured internal diameter of the lumen space within the vessels (Fig. 3A-3C).

In total, we examined 31 arteriole segments from eight mice to address this issue. Spontaneous contractions and dilations of arterioles were observed in both external and internal diameter kymographs (Fig. 3A-3C). Moreover, the time series of $\Delta D/D_0$ revealed high correlations between these two types of diameters (Fig. 3A-3D), and a 0.1-Hz peak was observed in the spectral analysis (Fig. 3E). Moreover, our findings showed no discernible differences in the vasomotion index (Fig. 3F). Based on these comparisons, we conclude that internal and external diameters can both be effectively utilized to investigate the properties of spontaneous vasomotion (Movie 4). This is particularly important when there is a need to

retrospectively compare features between data that have already been obtained solely from the external or internal diameter.

The radius vasomotion index reveals that the circular arteriolar wall does not isotropic contract and dilate in an isotropic manner.

In the kymograph and time series data analyses performed in this study (Figs. 1-3) as well as previously published representative kymographs of vasodynamics obtained under various conditions, including basal, neural, and chemical stimuli conditions[6], we observed that the two sides of the kymograph tended to be asymmetric (Figs. 2-3). Therefore, we developed a radius index to characterize this nonisotropic contractility of arterioles.

We determined the radius through three main steps. First, generate a midpoint line by dividing individual diameters by two (cyan line, Fig. 4A). Second, generate a centerline by fitting the midpoint line using the least-square method (yellow line, Fig. 4A), and it was considered as one endpoint of the radius. The other endpoint was the unilateral FWHM in time series, and then the radius was subsequently calculated.

Next, we verified that the internal and external radii, as well as the diameter, can be employed to investigate spontaneous vasomotion properties (Supplementary Fig. 4). To accomplish this, we compared the time series of each radius to that of the diameter and observed mismatched dilations and contractions (Fig. 4A). In contrast, mismatches between the external and internal radii were seldom observed (Fig. 4B, Movie 5).

Two types of disparities between the time-series curves should be considered: temporal disparities and amplitude differences. Thus, we examined the mismatches between the curves by combining the dynamic time warping (DTW) method with correlation coefficient (CC) analysis to gain a more comprehensive understanding of arteriolar wall movement. A higher DTW score signifies a greater distance (and thus less similarity) between two analyzed objects. The CC value did not reflect similarity in the amplitudes of the curves, as demonstrated by the constant R value as the amplitude decreased, while the DTW score increased with decreasing amplitude (Supplementary Fig. 5A-B). Similarly, when comparing the mathematically scaled-down external radius with the internal radius, the R value remained constant while the DTW score increased (Supplementary Fig. 5A-B). Therefore, the DTW score can reflect amplitude changes.

There are four sets of CC values of different length amplitude ratio were compared separately (Fig. 4C), The CC obtained from the external radius positively correlates with its corresponding internal radius (External Vs. Internal: 0.7074 ± 0.01140, $p<0.05$). Similarly, the CC values of diameter were positively correlates with its corresponding radius (Diameter Vs. Side1 radius: 0.7223 ± 0.01981, Diameter Vs. Side2 radius: 0.7455 ± 0.0182, $p<0.05$). In contrast, the side1 radius did not correlate with side 2 radius (Side1 radius Vs. Side2 radius: 0.1729 ± 0.04281, $p<0.05$). Moreover, the DTW score obtained by comparing the two radii corresponding to a single diameter (side 1 versus side 2) was significantly higher than that obtained by comparing the side 1 radius with its corresponding external radius (Fig. 4D and Supplementary Fig. 5). This finding supports the asymmetry between the opposite arteriole walls.

Despite this asymmetry, the radius analysis showed a peak at approximately 0.1 Hz, similar to the results of the diameter analysis (Fig. 4E). Additionally, the radius index was generally comparable to the diameter index, except for two parameters: percent of length changes ($\Delta L/L_0$) and absolute difference in the length changes (ΔL) (Fig. 4F). This difference in length can be

attributed to the fact that the radius is half of the diameter. Overall, these data highlight that the radius-based analysis has unique advantages over diameter-based analyses for particular study aims, such as the extraction of time delay between fluctuation SMC calcium and arteriolar vasomotion, which will be discussed in detail in the upcoming sections.

Venules exhibit spontaneous vasomotion and respond differently to anesthesia than arterioles.

To examine whether cerebral venules exhibit 0.1-Hz vasomotion, we performed a paired comparison of the same venules in mice in awake and anesthetized states; the latter state was induced by intraperitoneal administration of pentobarbital sodium (10 ml/kg) (Fig. 5A). If anesthesia could alter venular vasomotion properties, it would indicate cerebral venules have vasomotion to be altered in the first place. Additionally, it is known that anesthesia does not deplete arteriole spontaneous vasomotion but dilates the resting diameter[28, 42], but it is still unclear to what extent anesthesia can induce. Furthermore, the differential vasomotor responses of arterioles and venules to anesthesia have not been quantitatively characterized.

The results showed that 25 arteriole segments from four mice with diameters ranging from 21.87 µm to 74.46 µm and 20 venule segments from three mice with lumen sizes ranging from 30.62 µm to 135.38 µm were all dilated when the mice were deeply anesthetized (Fig. 5A-D). The average dilation rate of the resting diameter of the venules was slightly higher than that of the arterioles, with dilation rates of 33.10±3.173% and 30.90±2.384%, respectively (Fig. 5B and 5D). This may be related to the observed reduction in vasomotion amplitude revealed by the time series analysis (Fig. 5E-F).

Notably, Fourier spectral analysis revealed that venules in awake mice also displayed a characteristic ultraslow frequency peak at approximately 0.1 Hz and that venules had significantly smaller amplitudes than arterioles (Fig. 5F). The further reduction in the diameter in response to pentobarbital sodium supported the conclusion that the venule results were not simply noise in the baseline but a real biological event (Fig. 5F). However, when we used the D_0 average or D_0 minimal method instead of the D_0 smoothing method to determine the baseline, we did not detect any vasomotor activities in the venules.

Moreover, in general, the arteriole and venule motion frequencies both decreased under anesthesia. Specifically, the frequency of the venules decreased more (34.4%) than that of the arterioles (11.45%), and the interval between spreading depolarization (SD) events showed a similar trend. However, the amplitude-related properties of the arterioles decreased more than those of the venules, with reductions of 44.90±2.664% in $\Delta D/D_0$ and 25.15±4.739% in ΔD (Movie 6), as opposed to the reductions of 32.95±4.931% and 9.431±5.775% in the venules (Movie 7), respectively (Fig. 5G-H).

Consistent with previous reports, anesthesia did not deplete arteriole vasomotion but significantly reduced the power. Recently, arteriole wall motion was found to propagate along the vascular longitudinal axis[33]. Our study confirmed this propagation in arterioles and revealed that this propagation was robustly suppressed under the influence of anesthetics (Fig. 5I-L), suggesting a novel aspect of the side effects of anesthesia. Taken together, our findings demonstrate that anesthesia profoundly affects spontaneous vasomotion, with different impacts on arterioles and venules.

Vasomotion amplitude is inversely correlated with vessel resting diameter

Next, to emphasize lumen size-based differences in our subsequent analyses, the three

breakpoints were employed to categorize the vessels into four diameter ranks. These numbers corresponded to the quartiles value in normalized histograms for vessel segments, which were the natural point to divide the data[39]. For arterioles, 170 segments from sixteen mice were calculated, the 23.05 μm, 32.18 μm and 38.83 μm were breakpoints of the lower quartile diameter, median diameter and upper quartile, respectively. The ranks were defined as rank1 (38.83 < d < 56.31 μm), rank2 (32.18 < d < 38.83 μm), rank3 (23.05 < d < 32.18 μm), and rank4 (17.80 < d < 23.05 μm). For the venules, 112 segments from fifteen mice were analyzed, the ranks were defined as rank1 (67.13 < d < 139.61 μm), rank2 (50.62 < d < 67.13 μm), rank3 (34.14 < d < 50.62 μm), and rank4 (11.85 < d < 34.14 μm).

We then characterized the differences in the vasomotion indices between arterioles and venules of different ranks. Representative kymographs and $\Delta D/D_0$ time series appeared to indicate that the smaller vessels in both arteriolar and venular networks exhibited more pronounced vasomotion (Fig. 6A-D).

After a comprehensive analysis, we found no differences in the frequency or interval SD among arterioles and venules with different ranks. Intriguingly, the ΔD values of the arterioles were consistently approximately 2 μm, regardless of rank, while the ΔD values of the venules decreased from 1.47 μm to 0.8855 μm as the rank increased from 1 to 4. Therefore, when normalized to the gradually decreasing baseline D_0 from rank 1 to 4, the $\Delta D/D_0$ value gradually increased, doubling as the venule rank increased from 1 to 4 (Fig. 6E-F).

Additionally, we isolated and aligned individual vasomotion events (Fig. 6G-H). To our knowledge, this is the first time that the kinetics of single vasomotion events have been revealed. Our findings indicate that each cycle required approximately one second for both arterioles and venules to dilate and two and one second for arterioles and venules to contract, respectively. Ideally, as 0.1-Hz rhythmicity implies one event every 10 seconds, our findings suggest that the vessel wall remains still during the remaining six to seven seconds in each cycle. These analyses represent a comprehensive characterization of vasomotion features in arteriolar and venular networks.

Comparisons of the relationships between mural cell Ca^{2+} oscillations with vasomotions in arterioles and venules

Mural cells include arteriolar SMCs, capillary pericytes, and venular pericytes. To determine the role of Ca^{2+} oscillations in different mural cells in driving spontaneous vasomotion, we used awake *PDGFRβCreER:Ai96* mice, in which every type of mural cell expresses the genetically encoded Ca^{2+} probe GCaMP6s. Intraluminal injection of rhodamine into these mice allowed simultaneous measurements of Ca^{2+} oscillations and lumen diameter dynamics (Fig. 7A-B). We used the same baseline smoothing method to determine the baseline Ca^{2+} signal. Consistent with previous studies[6, 28], SMC Ca^{2+} dynamics were inversely correlated with arteriolar diameter changes (-0.4891±0.02710, 23 arteriole segments in 5 mice, Movie 8), while no correlation between venular Ca^{2+} dynamics and vasomotion was observed (-0.1240±0.04023, 21 venule segments in 5 mice, Movie 9) (Fig. 7C-E). If Ca^{2+} dynamics are the driver of vasomotion, Ca^{2+} oscillations should have a 0.1 Hz peak in the spectral domain. Indeed, we identified this peak in arteriole SMCs but not in venule pericytes (Fig. 7F-G).

Consistent with the established notion (Figure 6), arterioles fluctuated more prominently than venules, with larger $\Delta D/D_0$ and ΔD values. In contrast, the average frequency and interval SD were comparable between arterioles and venules (Fig. 7I). However, the $\Delta F/F_0$ and ΔF

values associated with SMC Ca^{2+} dynamics were smaller than those associated with venule pericyte Ca^{2+} changes (Fig. 7H). All these data indicate that in contrast to arteriole vasomotion, venule vasomotion is independent of pericyte Ca^{2+} waves and instead relies on other currently unknown drivers. These data demonstrate the differential relationships among vasomotion in different vascular segments and their corresponding mural cell Ca^{2+} oscillations.

To determine whether SMC Ca^{2+} dynamics drive arteriole vasomotion, we employed a high-speed line scanning approach at a > 100 Hz scanning rate to determine how early SMC Ca^{2+} activity leads to vasocontraction (Fig. 7J). The time series of changes in the diameter, radius, and Ca^{2+} activity revealed a clearly mirrored pattern between vasomotor activity and Ca^{2+} oscillations when a vasomotion event occurs (Fig. 7K). The CC value calculated between the changes in the diameter and GCaMP6s fluorescence intensity was -0.4040±0.07691 (Fig. 7L), which is close to previous findings[6]. Notably, we found a significantly higher correlation of -0.7684±0.02199 when we used the radius parameter to calculate the CC value. Furthermore, we found that SMC Ca^{2+} activity led to vasocontraction in 178.3±18.03 ms, which was nearly one-quarter of the time calculated using the diameter (762.9±128.1 ms) (Fig. 7M-N). Thus, we conclude that although the diameter and radius indices are interchangeable in most vasomotion analyses, when observing actual time delay result between SMC Ca^{2+} oscillations and vasomotion (Fig. 7J), radius-based vasomotion analysis has been shown to be able to more precise investigate the relationship between SMC Ca^{2+} oscillations and vasomotion.

During ischemic stroke, arteriole vasomotion impairment is an early pathology that persists for a long time.

We implemented transient (2 hours) filament occlusion of the middle cerebral artery (tMCAO) and performed in vivo repeated imaging of the same cerebral MCA branches before occlusion, during occlusion, and 1 or 14 days after recanalization. We used hydrazide 633 to label arterioles in genetically engineered mice. To capture SMC Ca^{2+} signals during the complete vasoconstriction cycle, we acquired one image of *SMACreER:Ai96* mice every 1.08 seconds throughout the entire 2-hour occlusion period in. We observed Ca^{2+} overload in SMCs, with signal amplitudes four times higher than basal levels (Fig. 8A-B). In addition, obvious nonisotropic movements between the two sides of the vascular wall were observed in the kymograph (Fig. 8A, Movie 10). These Ca^{2+} elevations were immediately followed by strong SMC constrictions. This led to a reduction in the resting diameter from 32.82 µm to 12.29 µm within 22 seconds and in the sequential fast and slow recovery phases, and recovery to baseline was not achieved within 200 seconds (Fig. 8A-B). These data suggest that SMC Ca^{2+} overload is likely the central pathological driver of arteriolar constriction. It has been established that the pathological progression differs between adult stroke and neonatal stroke[43-45]. In adult mice stroke model, vasomotion impairment has been observed during the MCAO period, may leading to the further vascular damage and impeding recovery. However, it remains unclear whether similar vasomotion impairment occurs in mouse pups. Here, the SIMPLE model was employed, which is a reliable technique for inducing focal ischemic stroke in mouse pups[46, 47]. Then we extracted the vessel diameter change within 43 minutes during SIMPLE period. Our findings revealed vasomotion impairment during the stroke period in moue pups, similar to what has been observed in adult stroke models (Movie 11). These results suggest that vasomotion impairment may be a common pathological feature across different age groups in stroke.

Multiple episodes of SD-induced vasoconstriction occur during ischemia[6, 48], and we

hypothesized that these early constrictions gradually lead to damaged vasomotion. To analyze basal vasomotion properties, we examined the time interval between two consecutive episodes, during which excessive Ca^{2+} overload dissipated, and the resting diameter stabilized for at least 7 minutes. For instance, we recorded three complete SD episodes, which occurred 5, 43, and 63 minutes after suture-mediated occlusion. Notably, we observed only slight and moderate deterioration 7 min after the first episode (MCAO 12 min) and 16 min after the second episode (MCAO 59 min), respectively, while we detected nearly no vasomotor activity (inert status) 52 min after the third episode (MCAO 1h55 min) (Fig. 8C-D). These findings indicate that during the super acute ischemia phase, repeated SMC Ca^{2+} overload has an immediate and accumulative detrimental impact on basal vasomotion.

In total, we examined six mice, each of which displayed 1–4 episodes and an average reduction in the resting diameter of $30.87 \pm 3.200\%$ (Fig. 9E-9F). Notably, we consistently observed impaired vasomotion following the initial vasoconstriction in five out of six mice (Fig. 9E). We may have missed the first vasoconstriction in the mouse represented by the peach-colored dots due to the blank four-minute period required to settle the animal under the microscope (indicated by the gray bar, Fig. 8E). Taken together, our findings indicate that spontaneous vasomotion impairment follows pathological arteriolar constriction driven by SMC Ca^{2+} overload during early ischemia.

Next, to determine the extent of vasomotion damage, we examined vasomotor activity at the same MCA branches that were previously imaged in the short-term and long-term periods after recanalization (Fig. 8G-I). The kymographs and time series generated at the same ROI as the indicated yellow line revealed that arterioles transitioned to an inert state and showed very mild recovery (Fig. 8G-H). The spectral density analysis revealed a similar trend (Fig 8I). In addition, the vasomotion indices of frequency and $\Delta D/D_0$ reached their lowest values approximately one day after recanalization and recovered only slightly 14 days after recanalization (Fig. 8J). These findings imply that the early constriction experienced by SMCs likely causes permanent impairment with limited potential for recovery. Our findings suggest that long-term vasomotion damage is a previously unrecognized vascular pathology associated with stroke that may impact postischemic blood flow. Consequently, targeting the early dysfunction of myogenic spontaneous vasomotion could be a novel therapeutic approach for preventing reperfusion deficits.

Discussion

In this study, we first examined spontaneous vasomotion in both arteriolar and venular networks in the mouse brain under various conditions, such as ex vivo, head-fixed awake, anesthesia, and focal ischemia. By adopting a time-rolling baseline method to investigate vasomotion (Fig. 1), we overcame long-standing challenges: we isolated single vasomotion events and identified venule vasomotion. Then, we comprehensively and quantitatively characterized thirteen aspects of vasomotion, including kymographs, the time series amplitude ratio, spectrum density, vasomotion indices (frequency, interval SD, ΔD, $\Delta D/D_0$ and resting average diameter), single vasomotion event kinetics, correlation and DTW relationships, vasomotion propagation, and the time latency between changes in SMC Ca^{2+} activity and vasomotion. For the first time, we considered the radius parameter in vasomotion, identifying asynchronous movement of the

vascular wall at transverse cross-sections (Fig. 4). Importantly, we identified a novel vascular pathology in which arterioles transitioned from a vasoactive to a vaso-inactive status following repeated SD-induced vasoconstrictions during the super acute ischemia period, with more SD episodes leading to more severe vasomotion damage (Fig. 8). Vasomotion can serve as a valuable indicator to assess the extent of vascular damage under ischemic stroke. Furthermore, interventions targeting vasomotion modulation may hold promise for decreasing the detrimental effects of stroke on brain. These detailed quantitative descriptions of spontaneous vasomotor activity improve our understanding of the basic functional features of cerebral vasculature and its progressive functional susceptibility to ischemia.

We measured the duration of single vasomotion events in both the arteriole and venule networks. The 3.24-second vasomotion events observed for arterioles are consistent with recent findings on the average duration of the coinciding SMC Ca^{2+} peak (~3 seconds)[28]. This consistency suggests that single events were reliably isolated in the present study and that SMC Ca^{2+} fluctuations influence vasomotion kinetics.

We split the vasomotion cycle of arterioles into two key phases: a shorter rising phase (1.08 seconds) and a longer declining phase (2.16 seconds) (Fig. 6D). In the future, a faster scanning frequency could be implemented, which may reveal smoother kinetics than the present slower planar scanning approach. Given that our measurements are reliable, it would be interesting to investigate why the decline phase of venule vasomotion is shorter than that of arterioles, as this might elucidate the basic difference between arteriole and venule physiology.

Most vasomotion research has focused on arterioles, and there is no consensus on whether cerebral veins and venules also exhibit vasomotion; moreover, there is no fundamental understanding of its functional significance and underlying mechanisms. Capillaries and venules both show less prominent vasomotor activity than arterioles, but most comparative studies have focused on the differences between arterioles and capillaries, rather than differences between arterioles and venules[6, 28]. Indeed, the $\Delta D/D_0$ value of venules is substantially smaller than that of arterioles (Fig. 7H), which may explain why venues are more difficult to detect. With the baseline smoothing method, we not only detected venule vasomotion events but also revealed a characteristic 0.1 Hz peak, resembling that of arterioles. However, this peak was completely attenuated by anesthesia, whereas that of arterioles remained (Fig. 7F). It is well known that anesthetics profoundly suppress gamma band neural electrical oscillations[49], and this oscillation is known to entrain cerebral vasomotion [15, 29], . Thus, this difference in the response to anesthesia strongly suggests that venule vasomotion largely depends on neural input.

In addition to basal neural input, SMC-based self-generated movement also generates arteriole vasomotion[29]. Our findings in ex vivo brains, in which presumably no neural activity was present after being in ACSF for two hours, support the role of the intrinsic contractility of SMCs in vasomotion generation (Fig. 2). However, how basal neural activity entrains venular vasomotion needs further exploration. Furthermore, although venular pericyte Ca^{2+} fluctuations were large (Fig. 7H), which is consistent with a recent finding that venular pericytes have large, asynchronous Ca^{2+} fluctuations[28], these fluctuations were not related to vasomotion. This implies that basal neural activity may drive venule vasomotion. However, the underlying mechanism linking neural activity with venules needs further exploration. These studies can include analyzing the impact of neural regulatory pathways on the constriction and dilation of

venules, as well as investigating the effect of neural signals on venular pericytes to provide a deeper understanding of the neurovascular coupling and vessel regulatory mechanisms.

Another finding in this study is that although venular pericyte Ca^{2+} fluctuations were large (Fig. 7H), which is in accordance with a recent finding that venular pericytes display large, asynchronous Ca^{2+} fluctuations[28], they had nothing to do with vasomotion at all. This further imply that basal neural activity may serve as the driver for venule vasomotion. However, what is underlying mechanism linking neural activity with venules needs further exploration.

Exploring the relationship between cerebrospinal fluid (CSF) flow and vasomotion is of utmost importance. From a dorsal view, CSF flow speed differs along the two sides of the pial arteriole wall, with faster flow on one side and slower flow on the other side[50]; however, the underlying mechanism remains elusive. Together with previous work suggesting that vasomotion promotes CSF flow, our findings on asymmetric movements of arteriolar walls (Fig. 4) may explain the asymmetry observed in CSF flow. Additionally, our findings of different vasomotion amplitudes across different ranks in the arteriolar network (Fig. 6) suggest potentially different potencies in CSF flow, which might lead to different spatial clearing rates of β-amyloid (Aβ). Indeed, studies on both AD patients and AD model animals have frequently reported that Aβ deposits do exhibit spatial differences related to the size of and distance between arteries and arterioles[51-53]. These results suggest that strategies to specifically manipulate and target arteriole segments should be developed in future work.

A limitation of this study is the low scanning rate of 0.926 Hz (< 1 Hz) when using a 512 × 512 FOV; as a result, we could obtain only the low-frequency domain in the vasomotor waves, which may lead to missing information. In the future, when using conventional TPLSM to study vasomotion, small FOVs, such as 128 × 128, that include only one vessel segment should be selected to capture higher frequency domains. Another limitation is that the analytical procedure is not sufficiently automated, and MATLAB code and considerable manual effort are needed to extract information related to vasomotion and calcium. To enhance automation and accuracy, reduce barriers to using the proposed method, and decrease labor costs, the software should be improved.

This study confirmed our recent findings that pial arterioles transition to an inert state during the first 24 hours after recanalization[54]. However, how early vasomotion damage is induced and how long vasomotion damage lasts have not yet been established. In the present study, we addressed these important questions by investigating the super acute period and a longer reperfusion period (RP 14 days) (Fig. 8) and found that the number of SDs appeared to have a cumulative effect on the extent of vasomotion damage (Fig. 8C). Therefore, we suspect that increased transient Ca^{2+} activity can cause more severe damage to molecular machines that are responsible for cyclic SMC contractility. Prevention of SMC Ca^{2+} overload could represent a novel therapeutic goal to prevent delayed damage to vascular function.

In conclusion, comprehensively quantifying vasomotion is essential for understanding cerebral vascular networks, assessing vascular healthy and exploring vasomotion therapeutic interventions. This quantitative approach enhances the knowledge of vessel dynamics, and ultimately contributes to the development of improved treatments for various brain disorders such as stroke, Alzheimer's disease and vascular dementia.

Materials and Methods

Animals

All animal protocols were approved by the Institutional Animal Care and Use Committee (IACUC) at Westlake University. The following mouse strains were used: wild type (C57BL/6J), *SMACreER*, *PDGFRβCreER*, *Ai14*, *Ai47*, *Ai96* (JAX:028866). All mice were bred and maintained in a specific-pathogen-free animal room on a 12-hour light-dark cycle and provided food and water ad libitum at Westlake University Laboratory Animal Resource Center (LARC). Except for one female mouse pups aged 11 days used in the SIMPLE-mediated dMCA occlusion ischemic stroke experiment, all other experiments used male and female mice offspring aged 2 to 6 months.

Experimental timeline

For breading the conditional reporter mice in mural cell, an efficient temporally-controlled transgenic mouse line, the SMACreER and *PDGFRβCreER* mice were used[55, 56]. For the tamoxifen-inducible Cre (CreER)-dependent conditional overexpression systems, we performed tamoxifen (MCE, Cat# HY-13757A/CS-2870) administration (15 mg/ml dissolved in corn oil, 3 mg daily for three consecutive days through intraperitoneal injection) and induction on adult mice, 3 weeks before in vivo imaging. After cranial window implantation, mice were allowed to recover for 2 weeks prior to imaging, to ensure that all surgery-related inflammation had resolved.

Anesthesia

For surgery and anesthetized two-photon imaging, mice were anesthetized with 1% pentobarbital sodium intraperitoneally (10 ml/kg for mice with a body weight of approximately 25 to 35 g). Core temperature was kept constant at 37°C using a homeothermic heating blanket system during all surgical and experimental procedures.

Cranial window surgery

After anesthetized with pentobarbital sodium, mice were maintained at a temperature of 37°C under a heating blanket throughout the cranial window surgery. A butterfly metal adaptor was first glued onto the skull with instance adhesive and dental cement, which was used for head fixation under 2PLSM. The cranial surgery was performed by drilling a 3-mm round window on the anterolateral parietal bone overlying the MCA territory. Afterward, the cranial window was sealed with a 3-mm round glass coverslip (Warner Instruments, CS-3R, Cat# 64-0720) with the instance adhesive (deli 502 super glue, Cat#No.7146).

Middle cerebral artery occlusion (MCAO) surgery

Focal cerebral ischemia was induced by the middle cerebral artery occlusion (MCAO) method as described previously[57]. Briefly, mice were laid on their backs and carefully placed on a 37°C heating blanket under a dissecting microscope. A surgical incision in the neck region was made to expose the right common carotid artery (CCA). After ligating the distal side and the proximal side of the CCA, a small incision was subsequently made between the two ligatures. Then, a silicon rubber-coated monofilament with a rounded tip (Diccol, Cat# 7023910PK5Re) was inserted intraluminally. The monofilament was introduced along the internal carotid artery until the origin of the MCA was occluded. The monofilament was left for 2 hours to prompt transient

focal cerebral ischemia. Afterward, reperfusion was performed by withdrawing the monofilament for another 22 hours.

SIMPLE-mediated dMCA occlusion ischemic stroke

Mouse pups were anesthetized with isoflurane and placed under a dissecting microscope with an animal surgery pad underneath the animal body. The skin of the surgical area around the face and head is disinfected with 75% alcohol. The dMCA can be seen through the semi-transparent skull at this early-age mice. Gently remove the superficial fascia of the skull above dMCA with a dry, sterile cotton swab and pre-load 20 μL of magnetic nanoparticles (MNPS, 10 mg/ml) in an insulin syringe. Once the micro-magnet has been fixed, inject MNPs for mouse pups (does, 80 mg/kg; volume, 10 ml/kg) with the pre-loaded insulin syringe via the superficial temporal vein. Then the superficial temporal is rapidly pressed with the dry cotton swab right after the withdrawal of the needle to stop bleeding. Afterward, the incision is sealed with the tissue adhesive gle. The duration of ischemia and reperfusion onset timing was controlled by when to remove micromagnets[46, 47].

Two-photon in vivo and ex vivo imaging

Mice were live-imaged using a two-photon laser scanning microscope (Olympus, FLUOVIEW, FVMPE-RS) equipped with a cooled high-sensitivity GaAsP PMT detector and an ultrafast IR pulsed laser system (Spectra-Physics, InSight X3, continuously variable wavelength range 680-1300nm). Pictures were acquired in a 512 × 512 pixels square with a 0.994-μm pixel size under a 25x water-immersion objective (Olympus, XLPLN25XWMP2, NA=1.05). During in vivo imaging measurements, the adult mice were imaged awake during daytime and allowed to move freely on a treadmill while being secured in place by fastening their head in a butterfly metal adaptor. For anesthesia live imaging, adult mice were anesthetized with 1% pentobarbital sodium, while mouse pups were anesthetized with isoflurane. Both groups were then head-fixed using a butterfly metal adaptor on a platform. The galvanometer scanner was used to take time-lapse images with a scan speed of 2 or 4 pixels per microsecond; in this way, the frequency of the frame scan images could be achieved as fast as 0.625-0.926 Hz. For vascular vasomotion detection in vivo, *SMACreER:Ai14*, *SMACreER:Ai47* mice were used to label the vascular walls. The vascular walls can also be labeled by the fluorescein dye Alexa Fluo633 hydrazide (ThermoFisher, Cat#A30634) through tail intravenous injection[58]. For mural cell cytosolic calcium detection in vivo, *SMACreER:Ai96* and *PDGFRβCreER:Ai96* mice (GCamp6s reported) were used. The mice vascular lumen was labeled by the fluorescent dye FITC-dextran (sigma, Cat#FD2000S, 10mg/ml) or RhoB-dextran (sigma, Cat#R9379, 10mg/ml) through tail intravenous injection. A 960 nm wavelength excitation was used navigate SMC (tdTomato or EGFP), calcium oscillation (GCamp6s) and vasculature (FITC, RhoB or Hydrazide 633). In MCAO models, the same region was detected before and after (Occ.2h, Rep.22h and Rep.14d) ischemic stroke with the frame scan mode under 2PLSM. During ex vivo imaging measurements, the dissected mouse brain was labeled by the Tetramethylrhodamine (TMRM) (ThermoFisher Cat#T668) in ACSF at 37℃ for two hours[59], then the SMC (TMRM positive mitochondria in SMC as the reference) was imaged at 960 nm wavelength under 2PLSM. For relationship research between calcium dynamics and vasomotion, the built-in line-scan mode of the two-photon microscope was used to take time-lapse information with a scan speed of 10

pixels per microsecond (0.994 μm/pixel, 100-200 Hz). For all the mice, time-lapse vascular changes in the same area under any intervention were fully recorded during the entire assay. All mice were maintained at a temperature of 37°C under a heating pad throughout the imaging process.

Vessel diameter and corresponding SMC Ca^{2+} signal measurement

All time-lapse pictures were analyzed in Fiji (version 2.3.0) and MATLAB (version R2021a; MathWorks) using custom-written scripts. SMC calcium, vascular diameter and radius were determined as described above from frame scan images collected at frequencies of 0.625-0.926 Hz or line-scan images collected at frequencies of 100-200 Hz. Measurements in which the awake mouse had substantially moved were excluded from further analysis. In the vessel-containing (Vascular wall labeled by *SMACreER:Ai14*, *SMACreER:Ai47* and Hydrazide 633 as external diameter, vascular lumen labeled by FITC and RhoB as internal diameter) images, ROIs were drawn on several vessel segments (on average 2-8 segments per FOV), where pixel brightness along a line orthogonal to the blood vessel was extracted. Image stacks in Tiff format were loaded into Matlab and then underwent gaussian filtering to reduce spatial noise. The diameter of the vessel (arteriole and venule) was determined as the full width at half maximum of the reslice profile[30], and the vessel mask of every time stack was created by brightness variation along horizontal pixels. The peak and valley intensity thresholds were determined visually for each image to ensure optical detection of the surface vessels. The parameters of the full width at half maximum (FWHM) were calculated by utilizing Monotone piecewise cubic interpolation (Pchip) developed by Hermite interpolation[60, 61]. The Pchip derived a necessary and sufficient condition for a cubic function to be monotonic on an interval, and these conditions are employed to develop an algorithm constructs an accurate, robust and visually pleasing piecewise cubic interpolant to data. The diameter change was obtained by sorting the diameter obtained by each time stack. In the calcium-signal-containing (*SMACreER:Ai96* and *PDGFRβCreER:Ai96*) images, regions of interest (ROIs) were drawn on several SMCs according to their outline (on average 2-8 per FOV), and the change in calcium signal under time series was reflected by changing of the average green fluorescence brightness of each SMC. The codes can be found at part 1 "1_Diameter_radius_detection" at https://github.com/JialabEleven/Vasomotion_analysis.

Vessel radius definition

For radius calculation, the midpoint line was generated by dividing individual diameter through two along the time series, based on the calculated FWHM (Figure 4(A)). In order to reduce the influence of errors in the data and extract a robust and appropriate radius boundary, an overdetermined linear system solved by the least-square method (LSM) is employed[62]. The LSM is probably the most popular technique in statistics due to several factors. Firstly, most common estimators can be casted within this framework. For example, the mean of a distribution is the value that minimizes the sum of squared deviations of the scores. Secondly, using squares makes LSM mathematically very tractable because the Pythagorean theorem indicates that, when the error is independent of an estimated quantity, one can add the squared error and the squared estimated quantity[63]. What's more, the mathematical tools and algorithms

involved in LSM have been well studied for a relatively long time. With one variable and a linear function, the prediction of centerline is given by the following equation:

$$\hat{Q} = m + nP \tag{1}$$

where a set of T pairs of observations $\{Q_i, P_i\}$ is used to find a function relating the value of the centerline Q (dependent variable) to the values of a midpoint line P (independent variable). m and n represents the intercept and the slope of the regression line, respectively. The least square method defines the estimate of these parameters as the values which minimize the sum of the squares between the measurements and the predicted values. The error ε is expressed as follows:

$$\varepsilon = \sum_{i=1}^{t}(Q_i - \hat{Q}_i)^2 = \sum_{i=1}^{t}[Q_i - (m + nP_i)]^2. \tag{2}$$

The estimation uses the property that a quadratic expression reaches its minimum value when its derivatives vanish. Taking the derivative of ε with respect to m and n, setting them to zero:

$$\frac{\partial \varepsilon}{\partial m} = 2n\sum_{i=1}^{t} P_i + 2\sum_{i}^{t} Q_i + 2tm \tag{3}$$

and

$$\frac{\partial \varepsilon}{\partial n} = 2n\sum_{i=1}^{t} {P_i}^2 + 2m\sum_{i}^{t} P_i - 2\sum_{i}^{t} P_i Q_i. \tag{4}$$

Solving the equations (3) and 4, the following least square estimates of m and n as:

$$m = \bar{Q} - n\bar{P} \tag{5}$$

and

$$n = \frac{\sum_{i=1}^{t}(P_i - \bar{P})((Q_i - \bar{Q})}{\sum_{i=1}^{t}(P_i - \bar{P})^2} \tag{6}$$

where $\bar{P}$ and $\bar{Q}$ represent the means of P and Q. LSM can be extended to more than on independent variable (employing matrix algebra) and to non-linear functions. The centerline is fitted by midpoint line using the least-square method above. The centerline was defined as one boundary of the side1 radius and side2 radius and the unilateral FWHM in time series as the other boundary for radius calculation, and eventually the radius was subsequently calculated. The codes can be found at part 1 “1_Diameter_radius_detection” at https://github.com/JialabEleven/Vasomotion_analysis.

Power spectrum analysis

Depending on the data format, power spectrum analysis was performed in MATLAB (text format) and presented the power spectral density on the y axis and frequency on the x axis according to shooting parameters. In MATLAB, Fast Fourier Transform (FFT) is employed to calculate the power spectral density of the arteriolar diameter (Figure 2D, 3E, 4E, 5F, 7F and 8I) radius (Figure 4E and S4B), venular diameter (Figure 5F and 7G) and mural cell calcium data (Figure 4E, 7F and 7G). The mice vasomotion and calcium signals under awake/anesthesia were sampled at 0.625 Hz or 0.926 Hz (FFT length: 200, the overlap: 50%), and the filtered power of the ultra-low frequency spectrum (0-0.3 Hz) was shown. The codes can be found at part 2 “2_Frequency_calculation” at https://github.com/JialabEleven/Vasomotion_analysis.

Pearson correlation coefficient and propagation index analysis

Previously, Pearson correlation coefficient (CC) and propagation analysis was implemented not only to identify the functional connectivity between ultra-slow single-vessel bold

spatiotemporal dynamics and neuronal intracellular calcium signals[31], but also to search spontaneous vasomotion propagates along pial arterioles in the awake mouse brain[33]. For this study, to investigate the interactions from one seed arteriolar vasomotion to other arteriolar vasomotion and relationship between vessels vasomotion and mural cell calcium, CC analysis was employed as an indicator of functional relationship. The definition of CC is as follows[64]:

$$\rho_{E,F} = \frac{\left[\sum_{j=1}^{n'}(E_i-\overline{E})(F_i-\overline{F})\right]/(n'-1)}{\sigma_E\sigma_F} \quad (7)$$

For functional relationship research between vessels vasomotion and mural cell calcium, n' indicates the length of signals (100-point length, 0.926 Hz). E represents the time series of vasomotion signal from vessel in one place, F represents the calcium time course signal of mural cell covered around vessel at this place. The $\overline{E}$ and $\overline{F}$ represent the mean values of the vasomotion signal and calcium signal, respectively. The σ_E and σ_F respectively represent the standard deviation of vasomotion signal and calcium signal.

As for the interactions investigation of vasomotion at different distances, n' indicates the length of signals (200-point length, 0.926 Hz), E represents the time series of vasomotion signal from one seed arteriolar, F represents the vasomotion time course signal from another arteriole. The $\overline{E}$ and $\overline{F}$ represent the mean values of the two vasomotion signals. The σ_E and σ_F represent the standard deviation of the two vasomotion signals. Along the arteriole, the core position is selected randomly, and the diameter change is calculated in this place with time stacks as core vasomotion. By choosing intervals of 2.5 μm, the vasomotion is calculated at each position ±30 μm from the core position. Compare the CC between each position vasomotion and the core position vasomotion, the corresponding curve can be obtained. To analyze the propagation of vasomotion under awake and anesthetized conditions in mice, multiple CC curves per vessel of various mice were summarized and averaged. In addition, the CC maps is shown as CC comparison of each vasomotion statistic position. The codes can be found at part 3 "3_Propagation_SMC" at https://github.com/JialabEleven/Vasomotion_analysis. The mashgrid 3D models, also called as the vasomotion synchronization 3D model, simultaneously presents the propagation parameters of time, distance, filtered amplitude ratio, and CC curve of vasomotion. The codes can be found at part 4 "4_3Dmodel_Synchronization" at https://github.com/JialabEleven/Vasomotion_analysis.

Time lag estimation between SMC calcium fluctuation and vasomotion

The datasets were simultaneously collected by high-speed line scanning at a frequency of 100-200 Hz using two-photon microscopy, resulting in a total of 2,000 serial frames for each dataset (Ca^{2+} signal U_{1-2000} and vasomotion signal V_{1-2000}). It is supposed that a cross correlation between two time series of SMC calcium dynamic U_N and arteriolar segment vasomotion V_N of equal length N ($N \ll 2000$, selected from U_{1-2000} and V_{1-2000}) exists obtained[65]. This vasomotion time series sliding window V_N was covered at least one vasomotion event. To estimate time lags, a set of cross-correlation coefficient T was conducted by sliding the Ca^{2+} signal U over the diameter or radius vasomotion V, with a forward-sliding step of one frame as interval. Firstly, the correlation coefficient ρ_{U_d,V_d} between SMC calcium dynamic U_d and arteriolar vasomotion V_d with a time series length of N starting from frame d is compared, which represents the relationship between two time series starting at same moment. Then keeping the vasomotion signal V_d unchanged, calculate the correlation coefficient ρ_{U_{d-1},V_d}

between the V_d and SMC dynamic signal U_{d-1} with a times series length of N at (d-1) frame. Following this pattern, the cross-correlation coefficient curve is obtained as follows,

$$T = \sum_{k=1} \rho_{U_{d-k+1}, V_d}. \quad (8)$$

Based on the results of SMC calcium dynamic and arteriolar vasomotion from time-lapse images, there is a negative cross-correlation between the two[6, 28]. The time lag between SMC calcium and arteriolar vasomotion was presented as the moment when cross-correlation curve arrived the minimum correlation (most negative correlation value). The codes can be found at part 5 "5_Time_lag_estimation" at https://github.com/JialabEleven/Vasomotion_analysis.

Dynamic time warping analysis

Dynamic time warping (DTW) is widely used as a similarity measurement to find an optimal alignment two given (time-dependent) sequences under certain restrictions[66]. It allows a non-linear mapping of one signal to another by minimizing the distance between the two. This measurement is the best solution known for time series problems in various domains, including bioinformatics[67], medicine[68], computer vision and computer animation[69], data mining and time series clustering[70-72] and signal processing[73]. Currently, DTW has earned its popularity by being extremely efficient as the time series similarity detection which minimizes the effects of shifting and distortion in time by allowing "elastic" transformation of time series in order to detect similar shapes with different phases.

Because of the universal adaptation and robust advantage of DTW in time series similarity comparison, this method can be combined with CC to describe the similarity of different vasomotion motion patterns. Here, based on the conclusion that both internal and external radius and diameters can be effectively utilized to investigate the properties of spontaneous vasomotion from Fig.3, the control group which means the same vasomotion motion patterns was defined as the paired DTW distance comparison between time series of internal and external diameter. Then the DTW distance between time series of side1 radius and side2 radius was calculated which had significant difference compared to the control group to give vital quantitative evidence that asymmetrical motion between the two sides of the arteriolar vasomotion.

Firstly, Given two time series $X = (x_1, x_2, \dots x_M)$ and $Y = (y_1, y_2, \dots y_M)$, $M \in \mathbb{N}$ represented by the sequences of vasomotion signals (200-point length). The restriction placed on the data sequences is that they should be sampled at equidistant points in time. Intuitively the DTW distance has a small value when sequences are similar and large value if they are different. The core of the DTW is the dynamic programming algorithm which is commonly called "cost" distance function. The task of optimal alignment of the sequences becoming the task of arranging all sequence points by minimizing the "cost" distance function. Algorithm starts by building the distance matrix $D \in \mathbb{R}^{N \times M}$ representing all pairwise distances between vasomotion signal time course X and Y. This distance matrix called the set of local cost matrix for the alignment of two sequences of X and Y:

$$D \in \mathbb{R}^{N \times M}: c_{i,j} = \|x_i - y_j\|, i \in [1:N], j \in [1:M] \quad (9)$$

the algorithm will find the alignment path which runs through the low-cost areas. This alignment path defines the correspondence of an element $x_i \in X$ to $y_j \in Y$ following the boundary condition which assigne first and last elements of X and Y to each other. The total cost function associated with warping path computed with sum of local cost matrix,

$$c_p(X,Y) = \sum_{l=1}^{L} c(x_{n_l}, y_{m_l}) \quad (10)$$

where n_l and m_l represent the path to arrive the next target. The warping path has a minimal cost associated with alignment called the optimal warping path called R^*. In order to find an optimal warping path, we need to test every possible warping path between X and Y which could be computationally challenging due to the exponential growth of the number of optimal paths as the lengths of X and Y grow linearly. To get over this challenge, the dynamic programming was employed,

$$DTW(X,Y) = c_{r^*}(X,Y) = \min\{c_r(X,Y), r \in R^{N\times M}\} \quad (11)$$

where DTW distance means the similarity description between two vessels time series motion curves (200-point length). The codes can be found at part 6 "6_CC_DTW_calculation" at https://github.com/JialabEleven/Vasomotion_analysis.

Calcium and vasomotion index calculation

For myogenic spontaneous vasomotion characterization, all data used for extracting the vasomotion index must follow a normal distribution. The vasomotion index was defined as the statistics on the total number of vasomotion events that exceeded the double standard deviation (SD) of the baseline[37]. The selection of baselines is the most critical step in analyzing calcium and vasomotion events. We determined F_0 by three different methods: calculating the mean value of diameter change time series curve (200-point length) as baseline which we will refer to as "F_0 average", calculating the minimal value of diameter change time series curve as baseline called "F_0 minimal" and finding the eighth smallest number in a forty sliding window producing a variable F_0 time series, referred to as the "F_0 smooth". The baselines of F_0 average and F_0 minimal were difficult to accurately detect total vasomotion events, while the baseline of F_0 smooth could objectively and ideally play a role (Figure S3). When the amplitude of vasomotion exceeded the double SD of the baseline, it is defined as a single event. The kinetic quantification index of events including the calcium index, diameter index, and radius index. These indexes all contained parameters of frequency, SD of peak intervals (interval SD), absolute amplitude and amplitude ratio, as follows:

$$\text{Frequency}: f = \frac{n_{events}}{\mathrm{t}_{total}} \quad (12)$$

$$\text{Interval SD}: S = \sqrt{\frac{\sum_h^H t_{\Delta e}}{H-1}} \quad (13)$$

$$\text{Absolute amplitude}: \Delta D(\Delta R, \Delta F) = D(R,F) - D_0(R_0, F_0) \quad (14)$$

$$\text{Amplitude ratio}: \frac{\Delta D(\Delta R, \Delta F)}{D_0(R_0, F_0)}. \quad (15)$$

Among them, frequency f means the all events (n_{events}) obtained according to the above judgment indicators divided by the total time stacks (t_{total}, 200-point length). The interval SD ($t_{\Delta e}$ represents the time interval between each two consecutive events and H represents the amount of events interval number) shows the stability of the time interval between two consecutive events. For the calcium index, when the calcium events come, the absolute amplitude represents the changes in GCamp6s fluorescence intensity (ΔF) of this time frame, and the amplitude ratio displayed as a change in calcium (ΔF) over baseline (ΔF_0) of this time frame. For the diameter or radius index, the average diameter calculated from the mean of total time diameter change stacks (200-point length), the absolute amplitude represents the change

in width values obtained from the two boundaries (ΔD or ΔR) when an event occurs, and the amplitude ratio indicates the change in width values (ΔD or ΔR) over baseline (ΔD_0 or ΔR_0). The inclusion criteria for the calcium events were similar as in the events selection in vasomotion. The codes can be found at part 7 "7_Vasomotion_index" at https://github.com/JialabEleven/Vasomotion_analysis.

Rank distribution of blood vessels

During analysis of surface arterioles, the three breakpoints were employed to categorize the vessels into four diameter ranks with locations at 23.05 μm, 32.18 μm and 38.83 μm. These numbers corresponded to the quartiles value in normalized histograms for arterioles segments (n=170 from sixteen mice), were the natural point to divide the data[74]. Further, 23.05 μm, 32.18 μm and 38.83 μm were the lower quartiles diameter, median diameter and upper quartiles diameter, respectively. For analysis of surface venules, the three breakpoints were 34.14 μm, 50.62 μm and 67.13 μm (n=112 from fifteen mice).

Quantification and statistical analysis

The numerical data concealed in the raw digital images were extracted and run on the software of Fiji (version 2.3.0/1.53f) or MATLAB (version R2021a). All statistical analyses and graphical illustrations were performed using GraphPad Prism 8 software (version 8.3.1, California, USA). All statistical tests were two-tailed, and significance was assigned at $p < 0.05$. Normality between group samples were assessed using the Kolmogrov-Smirnov test, Lilliefors test, Jarque-Bera test and Chi square Goodness-of-Fit test. When normality between sample groups was achieved, a paired Student's t-test were used. Pearson's correlation analysis was performed when normality of samples was achieved and the correlation values would only be recorded in the statistical data if the $p<0.05$. The data with error bars are displayed as the means ± SEM. No blinding and randomization design was needed in this work.

Conflict of interest

The authors declare no competing interests.

Acknowledgements

We are grateful to Jia-yu Ruan, Xu Hu, Xing-hua Quan for their technical contributions to this work. We are very grateful to Drs. Xu-zhang Li, Drs. Dong-dong Zhang and Drs. Zhu Zhu for constructive suggestions during the course of this study.

Author contributions

Yi-yi Zhang, Conceptualization, Resources, Data curation, Software, Formal analysis, Validation, Investigation, Visualization, Methodology, Writing – original draft; Jin-ze Li, Resources, Conceptualization, Data curation, Formal analysis, Validation, Investigation, Writing—review and editing; Hui-qi Xie, Resources, Conceptualization, Formal analysis; Yu-xiao Jin, Validation, Investigation; Wen-tao Wang, Investigation, Methodology; Bing-rui Zhao, Validation, Investigation; Jie-min Jia, Conceptualization, Funding acquisition, Project administration, Resources, Supervision, Writing review and editing

Funding

J.-M.J. acknowledges the support from Westlake University startup funding, the Westlake Education Foundation, Zhejiang Province Natural Science Foundation (Project # 2022XHSJJ004), and the National Natural Science Foundation of China (Projects# 31970969), Westlake Laboratory of Life Sciences and Biomedicine (Projects# 202309002), and The grants from National Natural Science Foundation of China Youth Programs of Projects# 82001267 to J.L.

Code availability

All image processing, analysis, and visualization, as detailed below, was performed in FIJI and MATLAB (MathWorks). The codes are divided into seven parts: Diameter radius detection, Frequency calculation, Propagation index calculation, 3D synchronization analysis, Time lag calculation, Dynamic time warping analysis and vasomotion index calculation.

All codes are available at https://github.com/JialabEleven/Vasomotion_analysis.

References

1. Mateo, C., Knutsen, P.M., Tsai, P.S., Shih, A.Y. & Kleinfeld, D. Entrainment of arteriole vasomotor fluctuations by neural activity is a basis of blood-oxygenation-level-dependent "resting-state" connectivity. *Neuron* **96**, 936-948. e933 (2017).
2. Noordmans, H.J. *et al.* Detailed view on slow sinusoidal, hemodynamic oscillations on the human brain cortex by f ourier transforming oxy/deoxy hyperspectral images. *Human Brain Mapping* **39**, 3558-3573 (2018).
3. Drew, P.J., Shih, A.Y. & Kleinfeld, D. Fluctuating and sensory-induced vasodynamics in rodent cortex extend arteriole capacity. *Proceedings of the National Academy of Sciences* **108**, 8473-8478 (2011).
4. Mayhew, J.E. *et al.* Cerebral vasomotion: a 0.1-Hz oscillation in reflected light imaging of neural activity. *Neuroimage* **4**, 183-193 (1996).
5. Osol, G. & Halpern, W. Spontaneous vasomotion in pressurized cerebral arteries from genetically hypertensive rats. *American Journal of Physiology-Heart and Circulatory Physiology* **254**, H28-H33 (1988).
6. Hill, R.A. *et al.* Regional Blood Flow in the Normal and Ischemic Brain Is Controlled by Arteriolar Smooth Muscle Cell Contractility and Not by Capillary Pericytes. *Neuron* **87**, 95-110 (2015).
7. Ursino, M., Cavalcanti, S., Bertuglia, S. & Colantuoni, A. Theoretical analysis of complex oscillations in multibranched microvascular networks. *Microvascular research* **51**, 229-249 (1996).
8. Cole, W.C., Gordon, G.R. & Braun, A.P. Cellular and ionic mechanisms of arterial vasomotion. *Smooth Muscle Spontaneous Activity: Physiological and Pathological Modulation*, 297-312 (2019).
9. Bakker, E.N., Sorop, O., Spaan, J.A. & VanBavel, E. Remodeling of resistance arteries in organoid culture is modulated by pressure and pressure pulsation and depends on vasomotion. *American Journal of Physiology-Heart and Circulatory Physiology* **286**, H2052-H2056 (2004).
10. Oishi, H. *et al.* Role of membrane potential in vasomotion of isolated pressurized rat

arteries. *Life sciences* **71**, 2239-2248 (2002).
11. Haddock, R., Hirst, G. & Hill, C. Voltage independence of vasomotion in isolated irideal arterioles of the rat. *The Journal of physiology* **540**, 219-229 (2002).
12. Auer, L. & Gallhofer, B. Rhythmic activity of cat pial vessels in vivo. *European Neurology* **20**, 448-468 (1981).
13. Jones, T.W. X. Discovery that the veins of the bat's wing (which are furnished with valves) are endowed with rythmical contractility, and that the onward flow of blood is accelerated by each contraction. *Philosophical Transactions of the Royal Society of London*, 131-136 (1852).
14. van Veluw, S.J. *et al.* Vasomotion as a Driving Force for Paravascular Clearance in the Awake Mouse Brain. *Neuron* **105**, 549-561.e545 (2020).
15. Mateo, C., Knutsen, P.M., Tsai, P.S., Shih, A.Y. & Kleinfeld, D. Entrainment of Arteriole Vasomotor Fluctuations by Neural Activity Is a Basis of Blood-Oxygenation-Level-Dependent "Resting-State" Connectivity. *Neuron* **96**, 936-948.e933 (2017).
16. Holstein-Rønsbo, S. *et al.* Glymphatic influx and clearance are accelerated by neurovascular coupling. *Nat Neurosci* **26**, 1042-1053 (2023).
17. Haidey, J.N. *et al.* Astrocytes regulate ultra-slow arteriole oscillations via stretch-mediated TRPV4-COX-1 feedback. *Cell Rep* **36**, 109405 (2021).
18. Gao, Y. & Raj, J.U. Role of veins in regulation of pulmonary circulation. *Am J Physiol Lung Cell Mol Physiol* **288**, L213-226 (2005).
19. Sakurai, T. & Terui, N. Effects of sympathetically induced vasomotion on tissue-capillary fluid exchange. *Am J Physiol Heart Circ Physiol* **291**, H1761-1767 (2006).
20. Welsh, M. *et al.* Androgen action via testicular arteriole smooth muscle cells is important for Leydig cell function, vasomotion and testicular fluid dynamics. *PloS one* **5**, e13632 (2010).
21. Lysiak, J.J., Nguyen, Q.A.T. & Turner, T.T. Fluctuations in rat testicular interstitial oxygen tensions are linked to testicular vasomotion: persistence after repair of torsion. *Biology of Reproduction* **63**, 1383-1389 (2000).
22. Collin, O., Zupp, J.L. & Setchell, B.P. Testicular vasomotion in different mammals. *Asian journal of andrology* **2**, 297-300 (2000).
23. Di Marco, L.Y., Farkas, E., Martin, C., Venneri, A. & Frangi, A.F. Is Vasomotion in Cerebral Arteries Impaired in Alzheimer's Disease? *J Alzheimers Dis* **46**, 35-53 (2015).
24. Anderson, G.K. *et al.* Peaks and valleys: oscillatory cerebral blood flow at high altitude protects cerebral tissue oxygenation. *Physiol Meas* **42** (2021).
25. Anderson, G.K., Sprick, J.D., Park, F.S., Rosenberg, A.J. & Rickards, C.A. Responses of cerebral blood velocity and tissue oxygenation to low-frequency oscillations during simulated haemorrhagic stress in humans. *Exp Physiol* **104**, 1190-1201 (2019).
26. Anderson, G.K. & Rickards, C.A. The potential therapeutic benefits of low frequency haemodynamic oscillations. *J Physiol* **600**, 3905-3919 (2022).
27. Aalkjær, C., Boedtkjer, D. & Matchkov, V. Vasomotion - what is currently thought? *Acta Physiol (Oxf)* **202**, 253-269 (2011).
28. Glück, C. *et al.* Distinct signatures of calcium activity in brain mural cells. *Elife* **10**, e70591 (2021).
29. Drew, P.J., Mateo, C., Turner, K.L., Yu, X. & Kleinfeld, D. Ultra-slow Oscillations in fMRI and

Resting-State Connectivity: Neuronal and Vascular Contributions and Technical Confounds. *Neuron* **107**, 782-804 (2020).

30. Shih, A.Y. *et al.* Two-photon microscopy as a tool to study blood flow and neurovascular coupling in the rodent brain. *Journal of Cerebral Blood Flow & Metabolism* **32**, 1277-1309 (2012).
31. He, Y. *et al.* Ultra-slow single-vessel BOLD and CBV-based fMRI spatiotemporal dynamics and their correlation with neuronal intracellular calcium signals. *Neuron* **97**, 925-939. e925 (2018).
32. Tong, L. *et al.* Imaging and optogenetic modulation of vascular mural cells in the live brain. *Nature Protocols* **16**, 472-496 (2021).
33. Munting, L.P. *et al.* Spontaneous vasomotion propagates along pial arterioles in the awake mouse brain like stimulus-evoked vascular reactivity. *Journal of Cerebral Blood Flow & Metabolism*, 0271678X231152550 (2023).
34. Fasano, A., Farina, A. & Caggiati, A. Modeling vasomotion. *Reviews in Vascular Medicine* **8**, 1-4 (2017).
35. Marshall, R.S. The functional relevance of cerebral hemodynamics: why blood flow matters to the injured and recovering brain. *Curr Opin Neurol* **17**, 705-709 (2004).
36. Harrison, M., Kendall, B., Pollock, S. & Marshall, J. Effect of haematocrit on carotid stenosis and cerebral infarction. *The Lancet* **318**, 114-115 (1981).
37. Neugornet, A., O'Donovan, B. & Ortinski, P.I. Comparative Effects of Event Detection Methods on the Analysis and Interpretation of Ca2+ Imaging Data. *Frontiers in Neuroscience* **15**, 620869 (2021).
38. Brozovich, F.V. *et al.* Mechanisms of Vascular Smooth Muscle Contraction and the Basis for Pharmacologic Treatment of Smooth Muscle Disorders. *Pharmacol Rev* **68**, 476-532 (2016).
39. Shih, A.Y. *et al.* Active dilation of penetrating arterioles restores red blood cell flux to penumbral neocortex after focal stroke. *J Cereb Blood Flow Metab* **29**, 738-751 (2009).
40. Fan, J.L. *et al.* High-speed volumetric two-photon fluorescence imaging of neurovascular dynamics. *Nature communications* **11**, 6020 (2020).
41. Fairfax, S.T. *et al.* Ca2+ signaling in arterioles and small arteries of conscious, restrained, optical biosensor mice. *Frontiers in Physiology* **5**, 387 (2014).
42. Kleinfeld, D., Mitra, P.P., Helmchen, F. & Denk, W. Fluctuations and stimulus-induced changes in blood flow observed in individual capillaries in layers 2 through 4 of rat neocortex. *Proc Natl Acad Sci U S A* **95**, 15741-15746 (1998).
43. Riel-Romero, R.M.S. Neonatal stroke. *Neurological Research* **30**, 839-844 (2008).
44. Revuelta, M. *et al.* Ischemic stroke in neonatal and adult astrocytes. *Mechanisms of Ageing and Development* **183**, 111147 (2019).
45. Fernández-López, D. *et al.* Blood–brain barrier permeability is increased after acute adult stroke but not neonatal stroke in the rat. *Journal of Neuroscience* **32**, 9588-9600 (2012).
46. Jia, J.-M. & Jin, Y. Modeling distal middle cerebral artery occlusion in neonatal rodents with magnetic nanoparticles or magnetized red blood cells, in *Neural Repair: Methods and Protocols* 55-65 (Springer, 2023).
47. Jia, J.-M. *et al.* Control of cerebral ischemia with magnetic nanoparticles. *Nature methods* **14**, 160-166 (2017).

48. Binder, N.F. *et al.* Vascular response to spreading depolarization predicts stroke outcome. *Stroke* **53**, 1386-1395 (2022).
49. Hudetz, A.G., Vizuete, J.A. & Pillay, S. Differential effects of isoflurane on high-frequency and low-frequency γ oscillations in the cerebral cortex and hippocampus in freely moving rats. *The Journal of the American Society of Anesthesiologists* **114**, 588-595 (2011).
50. Mestre, H. *et al.* Flow of cerebrospinal fluid is driven by arterial pulsations and is reduced in hypertension. *Nature communications* **9**, 4878 (2018).
51. Armstrong, R.A. Classic β-amyloid deposits cluster around large diameter blood vessels rather than capillaries in sporadic Alzheimer's disease. *Current Neurovascular Research* **3**, 289-294 (2006).
52. Robbins, E.M. *et al.* Kinetics of cerebral amyloid angiopathy progression in a transgenic mouse model of Alzheimer disease. *Journal of Neuroscience* **26**, 365-371 (2006).
53. Weller, R.O. *et al.* Cerebral amyloid angiopathy: amyloid β accumulates in putative interstitial fluid drainage pathways in Alzheimer's disease. *The American journal of pathology* **153**, 725-733 (1998).
54. Li, J. *et al.* Ca 2+ Oscillation in Vascular Smooth Muscle Cells Control Myogenic Spontaneous Vasomotion and Counteract Post-ischemic No-reflow. *Commun. Biol* **Under review** (2023).
55. Bondjers, C. *et al.* Microarray analysis of blood microvessels from PDGF-B and PDGF-Rβ mutant mice identifies novel markers for brain pericytes. *The FASEB journal* **20**, 1703-1705 (2006).
56. Wendling, O., Bornert, J.M., Chambon, P. & Metzger, D. Efficient temporally-controlled targeted mutagenesis in smooth muscle cells of the adult mouse. *Genesis* **47**, 14-18 (2009).
57. Koizumi, J., Yoshida, Y. & Nakazawa, T. A new experimental model of cerebral embolism in rats in which recirculation can be introduced in the ischemic area. Experimental studies of ischemic brain edema. *I. Jpn. J. Stroke*, 1-8 (1986).
58. Shen, Z., Lu, Z., Chhatbar, P.Y., O'herron, P. & Kara, P. An artery-specific fluorescent dye for studying neurovascular coupling. *Nature methods* **9**, 273-276 (2012).
59. Yokoyama, T. *et al.* Evaluation of the protective effects of cyclosporin A and FK506 on abnormal cytosolic and mitochondrial Ca2+ dynamics during ischemia and exposure to high glutamate concentration in mouse brain slice preparations. *Journal of pharmacological sciences* **120**, 228-240 (2012).
60. Kahaner, D., Moler, C. & Nash, S. *Numerical methods and software*. (Prentice-Hall, Inc., 1989).
61. Fritsch, F.N. & Carlson, R.E. Monotone piecewise cubic interpolation. *SIAM Journal on Numerical Analysis* **17**, 238-246 (1980).
62. Björck, Å. Least squares methods. *Handbook of numerical analysis* **1**, 465-652 (1990).
63. Abdi, H. The method of least squares. *Encyclopedia of measurement and statistics* **1**, 530-532 (2007).
64. Cohen, I. *et al.* Pearson correlation coefficient. *Noise reduction in speech processing*, 1-4 (2009).
65. Shen, C. Analysis of detrended time-lagged cross-correlation between two nonstationary time series. *Physics Letters A* **379**, 680-687 (2015).

66. Senin, P. Dynamic time warping algorithm review. *Information and Computer Science Department University of Hawaii at Manoa Honolulu, USA* **855**, 40 (2008).
67. Aach, J. & Church, G.M. Aligning gene expression time series with time warping algorithms. *Bioinformatics* **17**, 495-508 (2001).
68. Caiani, E.G. *et al.* in Computers in Cardiology 1998. Vol. 25 (Cat. No. 98CH36292) 73-76 (IEEE, 1998).
69. Müller, M. Dynamic time warping. *Information retrieval for music and motion*, 69-84 (2007).
70. Bahlmann, C. & Burkhardt, H. The writer independent online handwriting recognition system frog on hand and cluster generative statistical dynamic time warping. *IEEE Transactions on Pattern Analysis and Machine Intelligence* **26**, 299-310 (2004).
71. Niennattrakul, V. & Ratanamahatana, C.A. in 2007 International Conference on Multimedia and Ubiquitous Engineering (MUE'07) 733-738 (IEEE, 2007).
72. Gu, J. & Jin, X. in Intelligent Data Engineering and Automated Learning–IDEAL 2006: 7th International Conference, Burgos, Spain, September 20-23, 2006. Proceedings 7 841-848 (Springer, 2006).
73. Müller, M., Mattes, H. & Kurth, F. in ISMIR, Vol. 546 192-197 (Citeseer, 2006).
74. Shih, A.Y. *et al.* Active dilation of penetrating arterioles restores red blood cell flux to penumbral neocortex after focal stroke. *Journal of Cerebral Blood Flow & Metabolism* **29**, 738-751 (2009).

Figures

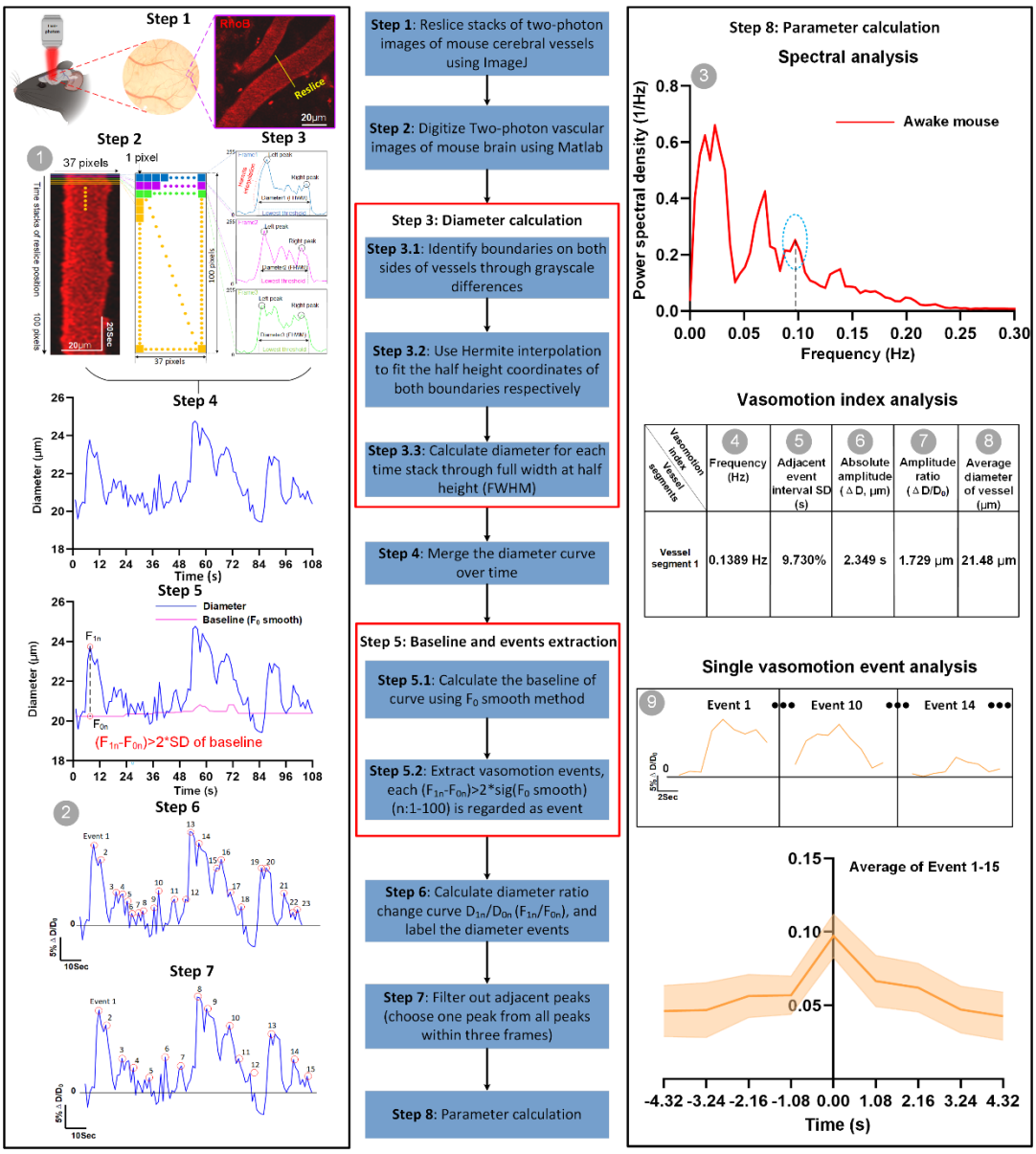

Figure.1 Flow chart of developing a comprehensive index for quantitatively and precisely characterizing spontaneous vasomotion. In vessel-containing images, time stacks of line ROIs are drawn on several vessel segments (The yellow solid line represents the reslice position, on average 2-8 segments per FOV), where pixel brightness along a line orthogonal to the length of the blood vessel was extracted. Image stacks in Tiff format are loaded into Matlab and total nine vasomotion parameters are output (The grey number ball indicates the detailed information of each parameter). These parameters are numbered in numerical order, representing as kymograph (1), time series diameter change curve (2), spectral analysis of diameter change curve (3), frequency of vasomotion (4), the standard deviation (SD) of interval times between two adjacent events (5), the absolute difference in vascular diameter change (6), the amplitude of difference in vascular diameter change (7), the amplitude ratio of vasomotion (8), the average diameter of vessel of time series and analysis of single events (9), respectively. All the results are exported into Excel.

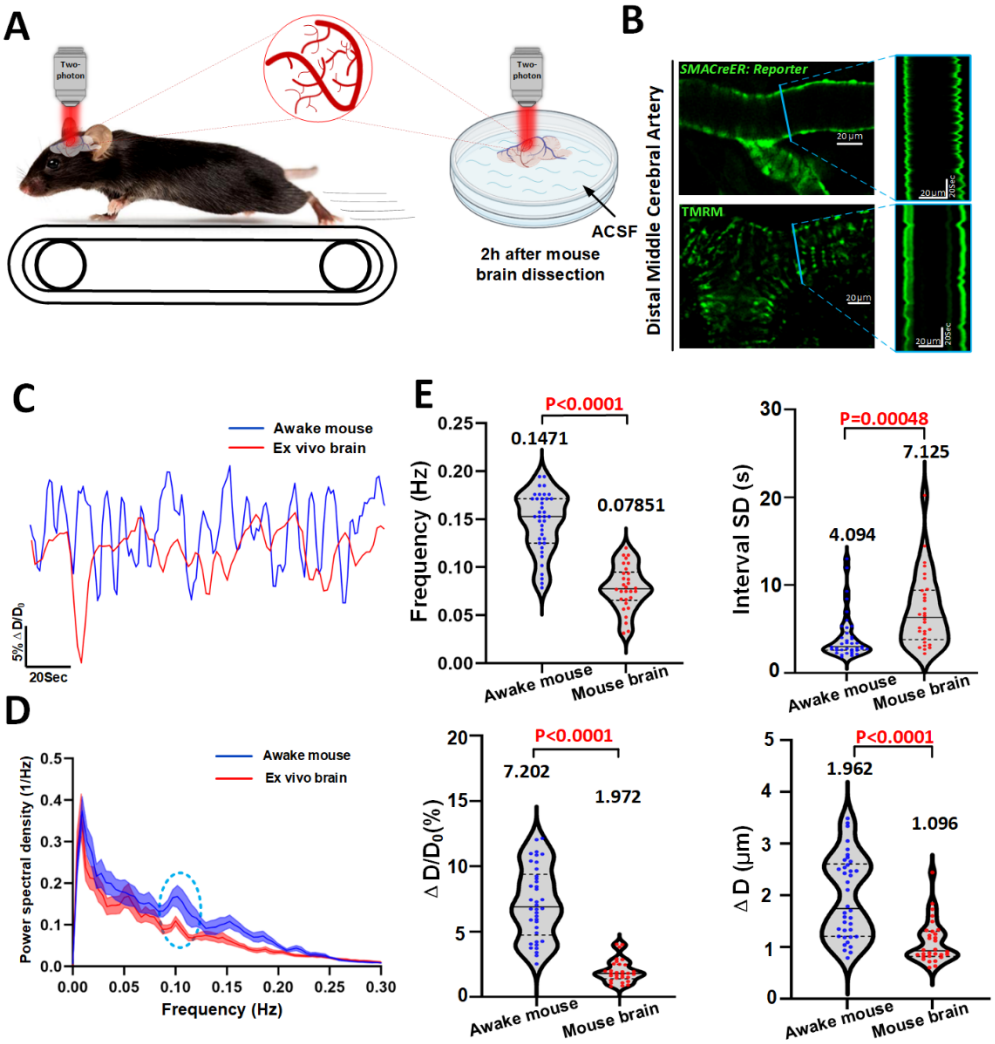

Figure.2 Vasomotion index analyses reveal freshly dissected mouse brains exhibiting altered but noticeable arteriolar spontaneous vasomotion compared to awake mouse brains. (A) Experimental design of the spontaneous vasomotion detection in awake mouse and ex vivo mouse brain. (B) Representative still-frame in vivo two-photon (2P) microscopy images and kymographs of cerebral arteriole through a cranial window in an awake head-fixed mouse and ex vivo mouse brain. The blue solid line represents the resliced position. (C) Representative time-series amplitude ratio ($\Delta D/D_0$) changes trace of awake mouse arteriole (blue solid line) and ex vivo mouse brain arteriole (red solid line). (D) The averaged Fourier plot across awake mouse cerebral diameter change and ex vivo mouse brain cerebral diameter change (n=15 arterioles segments in 4 awake mice) revealed a broad range of ultra-low frequencies (<0.3Hz), with a distinct peak centered at around 0.1 Hz. Shaded areas represent SEM. (E) Vasomotion index analysis between awake mouse (n=38 arterioles segments in 4 awake mice) and ex vivo mouse brain (n=30 arterioles segments in 4 mouse brains). Top left represents frequency of vasomotion, top right represents the SD of interval times between two adjacent events (interval SD), bottom left represents the amplitude ratio $\Delta D/D_0$ of vasomotion and bottom right represents the absolute difference in vascular diameter change ΔD.

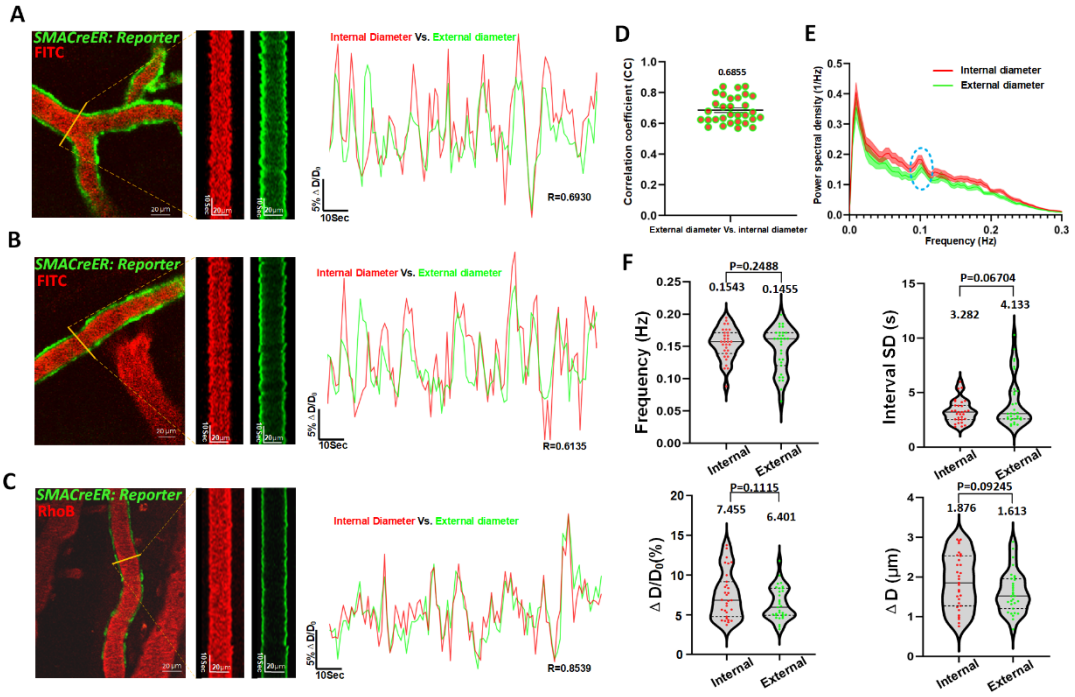

Figure.3 All dynamic changes in internal and external vascular diameter can be used to characterize spontaneous vasomotion. (A)-(C) Representative three levels still-frame images and kymographs of the same cerebral arteriole internal (red) and external (green) diameter and corresponding medium, low and high correlation coefficient (CC) of time-series external-internal diameter amplitude ratio $\Delta D/D_0$ changes curves, respectively. The yellow solid line represents the reslice position. (D) Quantification of CC values between same arterioles segments internal and external diameter vasomotion (n=31 arterioles segments in 8 awake mice). (E) The averaged Fourier plot across awake mouse cerebral internal and external diameter change of same arterioles (n=31 arterioles segments in 8 awake mice) revealed a broad range of ultra-low frequencies (<0.3Hz), with a distinct peak centered at around 0.1 Hz. Shaded areas represent SEM. (F) Vasomotion index analysis of cerebral arteriole between internal and external diameter (n=31 arterioles segments in 8 awake mice). Top left represents the index of frequency, top right represents the SD of the adjacent vasomotion event interval, bottom left represents the index of amplitude ratio $\Delta D/D_0$ and bottom right represents index of absolute amplitude ΔD. The reporter mice used in our study included Ai14, Ai47, and Ai96 mice which external diameter are uniformly labeled as green color and internal diameter are labeled as red color.

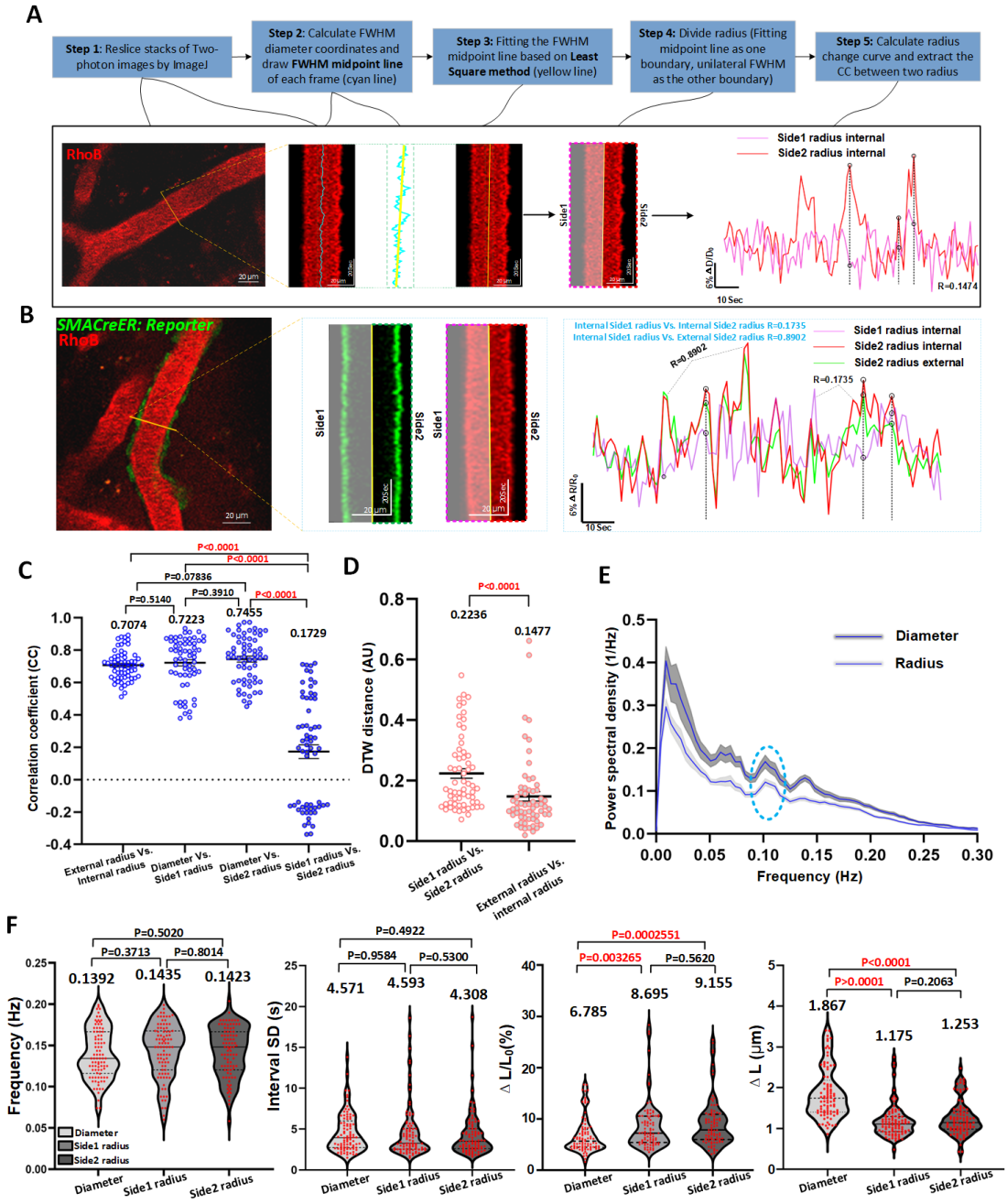

Figure.4 Radius vasomotion index reveals an asymmetrical movement between the two sides of the arteriolar wall at the maximum diameter section. (A) Flow chart of radius boundary definition. The yellow solid line represents the reslice position and the black dotted line represents the mismatched vasomotion. (B) Representative still-frame image and kymograph of cerebral arteriole internal (red) and external (green) radius. Right shows the CC values comparison of side1 radius and side2 radius amplitude ratio with internal and external radius amplitude ratio as reference. Shaded areas represent radius of the other side. (C) The statistic graph of CC value comparison reveals the correlation between internal and external radius amplitude ratio (n=62 arterioles segments in 8 awake mice), diameter and side1 radius (n=62 arterioles segments in 9 awake mice), diameter and side2 radius (n=62 arterioles segments in 9 awake mice), side1 radius and

side2 radius (n=62 arterioles segments in 9 awake mice). (D) Dynamic time warping (DTW) comparison reveals the difference of time-series radius change ratio curves between side1 and side2 radius (n=62 arterioles segments in 9 awake mice) of the same cerebral arteriole with internal and external radius (n=62 arterioles segments in 8 awake mice) as reference. (E) The averaged Fourier plot comparison across diameter (n=31 arterioles segments in 9 awake mice) and radius (n=62 arterioles segments in 9 awake mice) in awake mouse revealed a broad range of ultra-low frequencies (<0.3Hz), with a similar distinct peak centered at around 0.1 Hz (Blue round solid line). Shaded areas represent SEM. (F) Vasomotion index analysis between diameter and radius (n=89 arterioles segments in 9 awake mice).

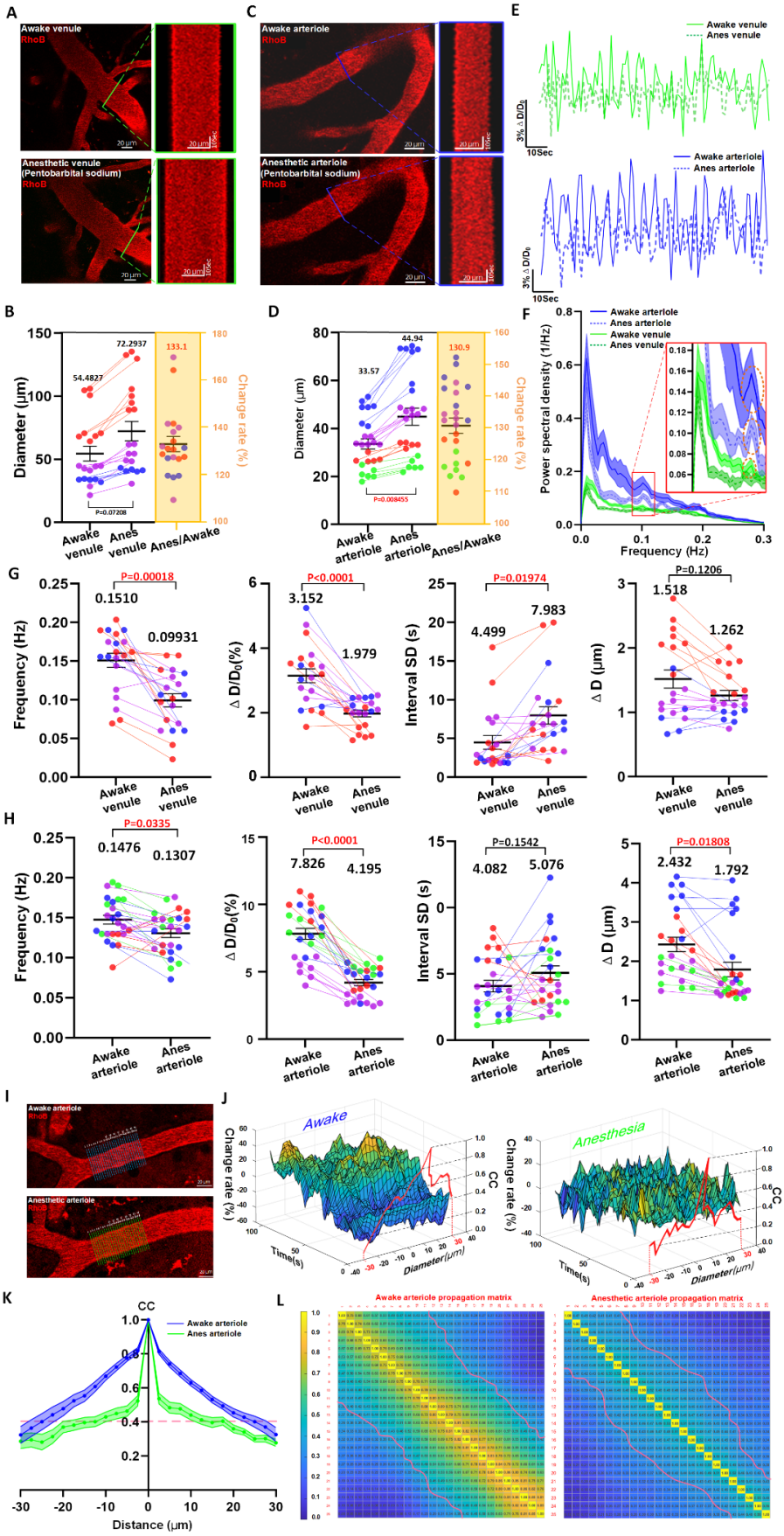

Figure.5 Anesthesia robustly dampens spontaneous vasomotion. (A) Representative

still-frame image and kymograph of same mouse venule in both awake and anesthetized states. The blue solid line represents the reslice position of awake mice and the green solid line represents the reslice position of anesthetized mice. (B) Cerebral venule dilation in mice (n=20 venules segments in 3 mice) under anesthesia. (C) Representative still-frame image and kymograph of same mouse cerebral arteriole in both awake and anesthetized states. (D) Cerebral arteriolar dilation in mice (n=25 arterioles segments in 4 mice) under anesthesia. (E) Representative time-lapse amplitude ratio change trace of same mouse venule (green) and arteriole (blue) in both awake (green and blue solid line) and anesthetized (green and blue dashed line) states. (F) The averaged Fourier plot across same mouse venule (green) and arteriole (blue) diameter change in both awake and anesthetized states (n=12 arterioles segments in 4 mice and n=18 venules segments in 3 mice)) revealed a distinct peak centered at around 0.1 Hz, while no significant peak in anesthetized mouse venule. Shaded areas represent SEM. (G)-(H) Vasomotion index comparison of same mouse venules and arterioles before and after anesthesia ((n=25 arterioles segments in 4 awake mice and n=20 venules segments in 3 awake mice). The different color dots represent different mice and connecting lines represent diameter or vasomotion index change of the same arteriole in the same mouse before and after anesthesia. (I) Representative example of the diameter change propagation dataset of same mouse cerebral arteriole in both awake and anesthetized states (J) Representative 3D mashgrid plots of arterioles before and after anesthesia. (K) The arteriolar diameter change propagation index analysis (see Methods). The blue (awake) and green (anesthesia) curves show the average cross-correlation value of different distance diameter change time-profile (n=21 arteriolar diameter change propagation column in 3 mice). The magenta dash line indicates correlation coefficient is 0.4. Shaded areas represent SEM. (L) The arteriolar diameter change propagation cross-correlation matrix (n=21 arteriolar diameter change propagation column in 3 mice, see Methods). The magenta dash line indicates correlation coefficient is 0.4.

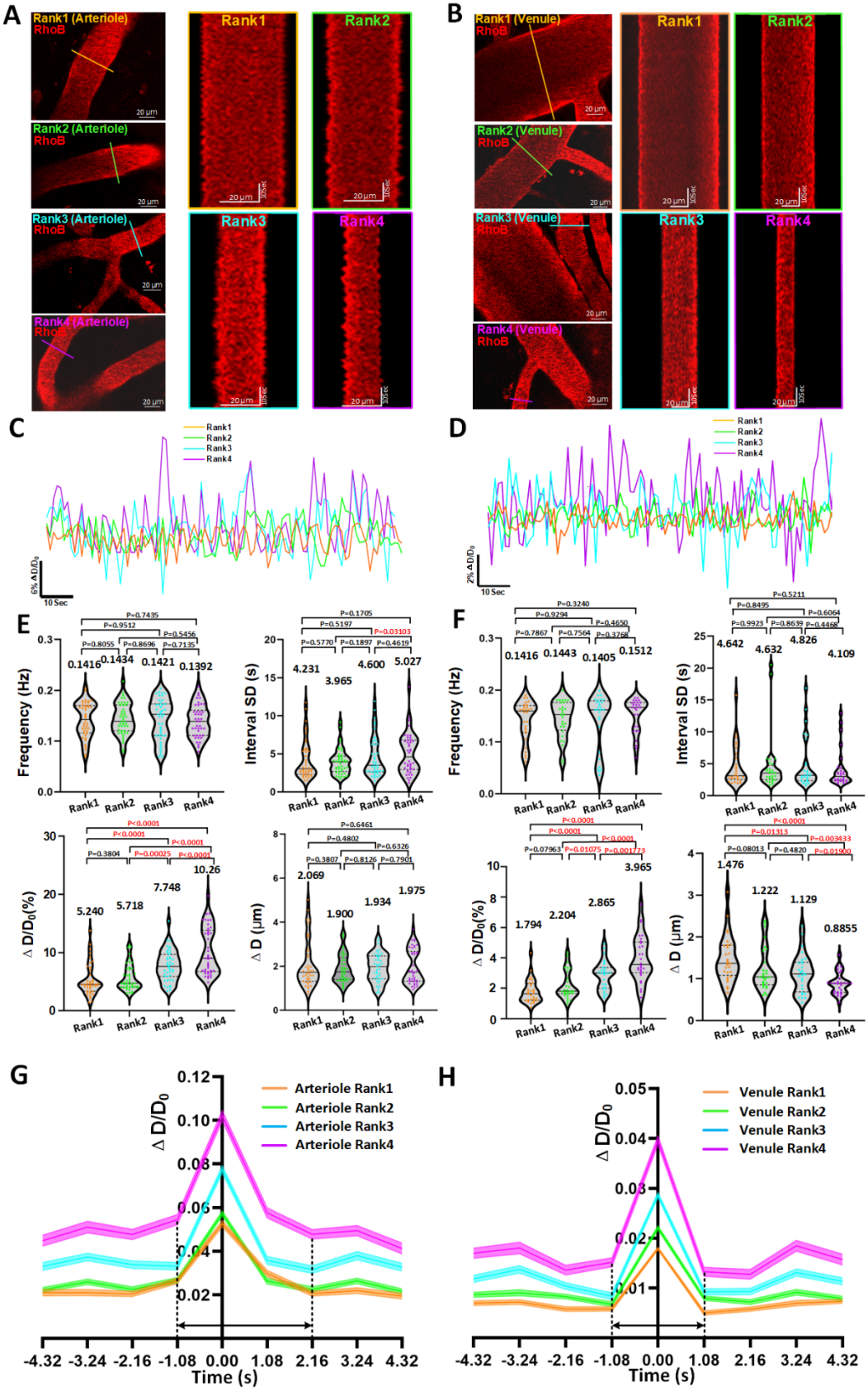

Figure.6 Differential features of spontaneous vasomotions crossing different levels in the arteriolar and venular networks. (A)-(B) Representative still-frame image and

kymograph of different rank cerebral arterioles (left) and venules (right). (The yellow, green, blue and purple solid line represents the line reslice position of rank 1-4, respectively). The 170 arteriole segments collected from 16 awake mice and 112 venules segments collected from 15 awake mice were ranked by Quartile distribution of diameter, respectively. For arterioles, Rank1: 38.85-56.31 μm (n=42 arterioles segments in 11 awake mice), Rank2: 32.18-38.85 μm (n=43 arterioles segments in 8 awake mice), Rank3: 23.05-32.18μm (n=43 arterioles segments in 10 awake mice), Rank 4: 17.80-23.05 μm (n=42 arterioles segments in 7 awake mice). For venules, Rank1: 67.13-139.64μm (n=28 venules segments in 11 awake mice), Rank2: 50.62-67.13μm (n=28 venules segments in 9 awake mice), Rank3: 34.14-50.62μm (n=28 venules segments in 9 awake mice), Rank 4: 11.84-34.14μm (n=28 venules segments in 11 awake mice). (C)-(D) Comparison of representative time-series amplitude changes trace at four diameter rank levels of arterioles and venules, respectively. (E)-(F) Vasomotion index comparison of arterioles (left) and venules (right) at four diameter ranks (n=170 arterioles segments in 16 awake mice and n=112 arterioles segments in 15 awake mice). (G)-(H) The averaged single vasomotion events plot comparison of arteriole (left) and venules (right) at four diameter ranks. For arterioles, Rank1: n=481 vasomotion events in 7 awake mice, Rank1: n=486 vasomotion events in 5 awake mice, Rank3: n=510 vasomotion events in 6 awake mice, Rank4: n=493 vasomotion events in 5 awake mice. For venules, Rank1: n=502 vasomotion events in 7 awake mice, Rank1: n=510 vasomotion events in 7 awake mice, Rank3: n=484 vasomotion events in 6 awake mice, Rank4: n=496 vasomotion events in 7 awake mice. Shaded areas represent SEM.

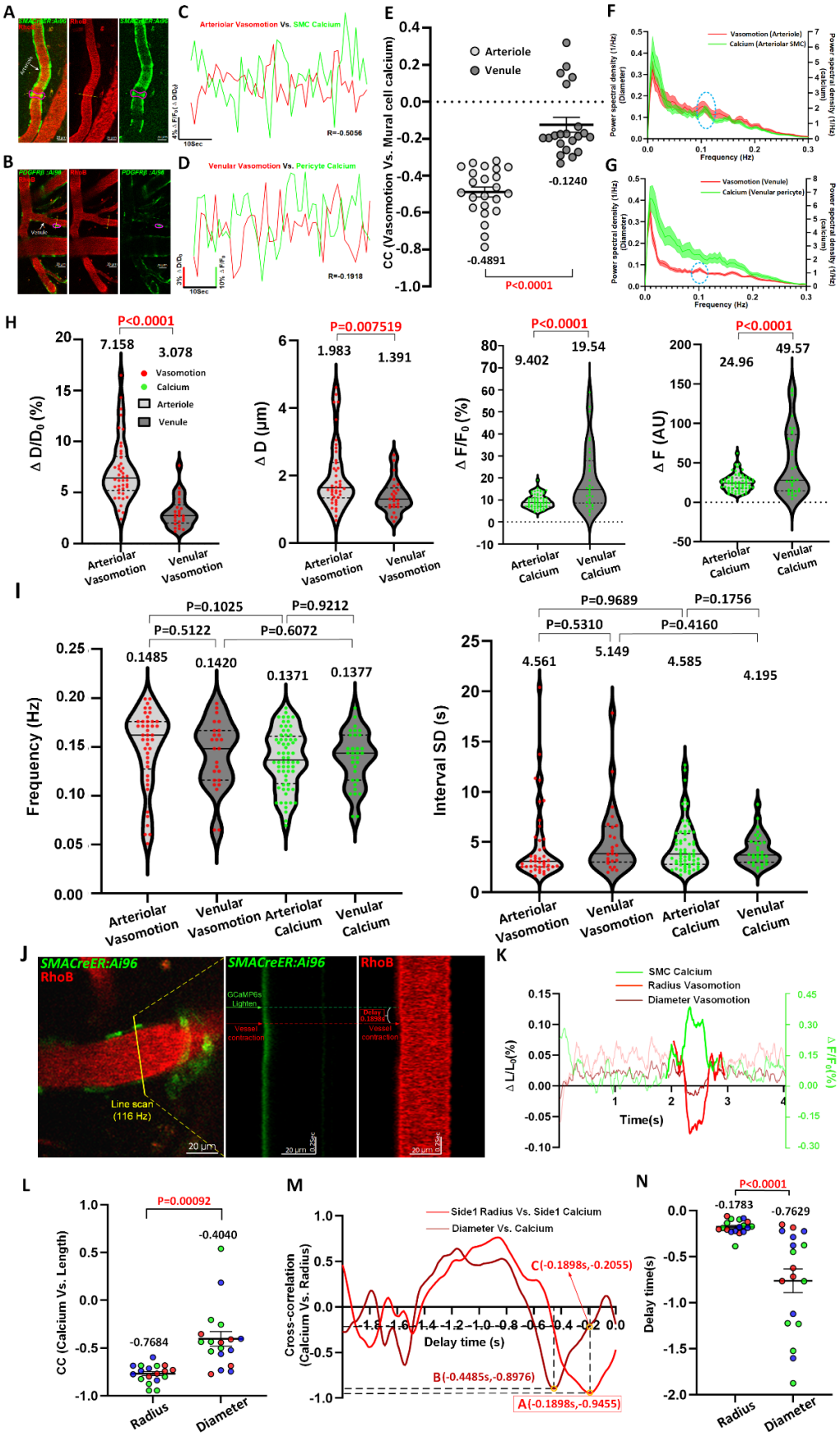

Figure.7 Mural cell calcium dynamics in vivo and the correlation between the calcium

signal with vessel vasomotion signal. (A)-(B) Representative still-frame images including vessels vasomotion (yellow line) and GCaMP6s calcium fluorescence intensity (green) changes of corresponding mural cell (purple mural cell shape curve). Calcium dynamic in mural cell was reported using *SMACreER:Ai96* mice or *PDGFRβ:Ai96* mice. (C)-(D) Representative time-series mural cell calcium amplitude ratio ($\Delta F/F_0$, green solid line) and vessels vasomotion amplitude ratio ($\Delta D/D_0$, red solid line) change traces of awake mouse, and the CC comparison of the two time series curves. (E) Left shows the quantification of CC values between arteriolar vasomotion and SMC calcium (n=23 pairs in 5 awake mice), right shows the quantification of CC values between venular vasomotion and pericyte calcium (n=21 pericytes in 4 awake mice). (F)-(G) The averaged Fourier plot across mouse vessel mural cell calcium signal change and vessel diameter change in awake state revealed a distinct peak centered at around 0.1 Hz, while no significant peak in venular pericyte calcium signal (n=38 SMCs in 6 awake mice Vs. n=21 arterioles segments in 6 awake mice, n=32 pericytes in 5 awake mice Vs. n=24 venules segments in 4 awake mice). Shaded areas represent SEM. (H)-(I) Mural cell calcium index and vessel vasomotion dynamic index in arteriolar SMCs calcium (n=64 SMCs in 5 awake mice), venular pericyte calcium (n=32 pericytes in 5 awake mice), arteriolar vasomotion (n=42 arteriole segments in 5 awake mice) and venular vasomotion (n=25 venule segments in 4 awake mouse) (J) Representative still-frame image and kymograph of cerebral arteriole using high frequency line scan. (K) Representative time series of calcium fluorescence ratio $\Delta F/F_0$, diameter amplitude ratio $\Delta D/D_0$ and radius amplitude ratio $\Delta R/R_0$ for one arteriole (J) in the field. (L) Left shows quantification averaged minimum cross correlation values comparison across arteriolar radius with SMC calcium, Right shows quantification averaged CC values when arteriolar diameter amplitude ratio with SMC calcium amplitude ratio lives up to time delay value corresponding to arteriolar radius and SMC calcium amplitude ratio (n=18 arterioles segments in 3 awake mice, different color dots represent different mouse). (M) The cross-correlation to determine the delay time between time series of calcium amplitude ratio and radius or diameter amplitude ratio used for the example in (J). The radius lags electrical activity (minimum of cross correlation) by 0.1898 s and the diameter lags electrical activity by 0.4485 s. (N) The quantification averaged delay time comparison across arteriolar radius or diameter with SMC calcium (n=18 arterioles segments in 3 awake mice, different color dots represent different mouse).

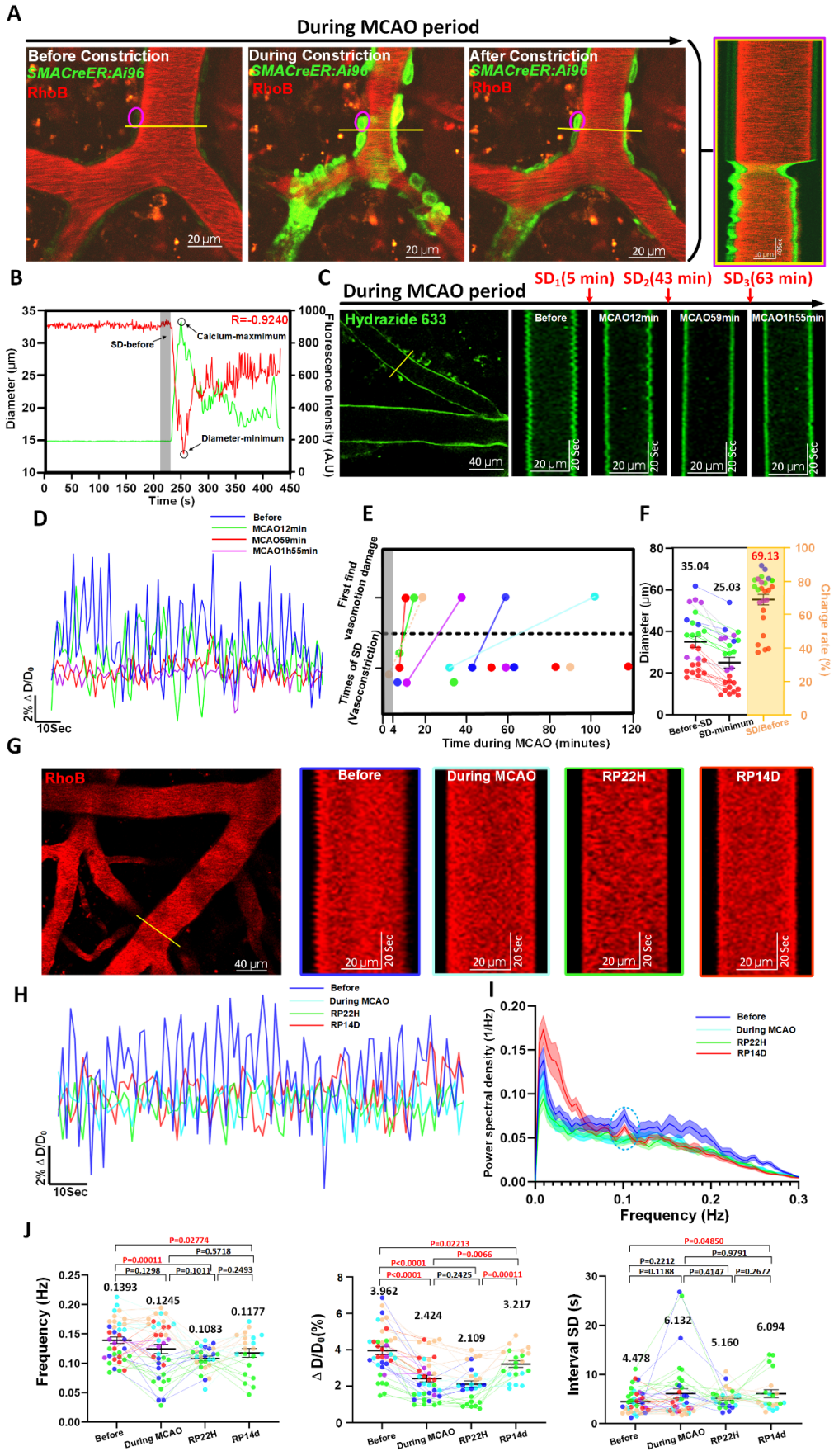

Figure.8 Vasomotion damage immediately takes place after the vasoconstriction during

the initial minutes of occlusion and lasts long despite successful recanalization. (A) Time-series sequence and kymograph showing both GCaMP6s calcium changes in a single SMC and cerebral arteriole diameter change undergoing spread depolarization (SD) vasoconstriction during MCAO period. The yellow line represents the reslice position. (B) Representative time-series calcium signal and diameter change trace of cerebral arteriole in anesthetized mouse during MCAO period. Shaded areas represent average diameter of 15 frames (16.2s) before SD. (C) Time-series sequence and kymograph showing the degree of vasomotion damage during the occurrence of SD in MCAO period. (D) Representative time-series amplitude changes trace of same cerebral arteriole during different stroke periods. (E) Top shows the first time vasomotion damage observed during MCAO period (N=6 anesthetic mice). Bottom shows times of SD within 4-120 minutes of MCAO (n=14 in 6 anesthetic mice). The gray column represents the time (4 minutes) taken for the mouse to 2P platform for imaging after MCAO surgery. The connecting solid lines represent time interval between vasomotion damage happening and first SD occurred during in vivo imaging recorded (the dashed line is estimated time interval). (F) Cerebral arteriolar vasoconstriction in mice (n=25 arterioles segments in 6 mice) under anesthesia. (G) Representative still-frame image and kymographs of same cerebral arteriole during different stroke periods. (H) Comparison of representative time-series amplitude changes trace of same arteriole at four periods (Before, During MCAO, RP22H and RP14D). (I) The averaged Fourier plot across same mouse cerebral arteriole diameter change at four stages (n=26 arterioles segments in 6 mice of before stroke stage, n=26 arterioles segments in 6 mice of during MCAO stage, n=20 arterioles segments in 4 mice of RP22H stage and n=17 arterioles segments in 3 mice of RP14D stage) revealed a distinct peak centered at around 0.1 Hz of stage before and RP14D, while no significant peaks of stage during MCAO and RP22H. Shaded areas represent SEM. (J) Vasomotion index comparison of same arterioles at four stages (n=37 arterioles segments in 6 anesthetic mice of before stroke stage, n=37 arterioles segments in 6 mice of MCAO damage stage, n=27 arterioles segments in 4 mice of RP22H stage and n=21 arterioles segments in 3 mice). Due to the partial death of stroke mice and decrease in imaging effect of the cranial window, the number of kinetics characteristics detecting mice decreases over time. The different color dots represent different mice and connecting lines represent diameter or vasomotion index change of the same arteriole in the different stages during stroke.